Politecnico di Torino

Nanotechnologies for ICTs

Master's Thesis Project

ELECTRICAL SIMULATION AND SYNTHESIS OF SEMI-CONDUCTIVE NANOFIBERS FOR THE STIMULATION OF OSTEOBLASTS

Candidate:
Gabriele Bongiovanni
S240284

Supervisors:
Prof. Gianluca Ciardelli
Prof. Chiara Tonda Turo

Supervisors in the Host Institution:
Dr. Annina Steinbach
Dr. Thomas Winkler
Dr. Derrick Roberts

September 2018

Gabriele Bongiovanni: *Electrical simulation and synthesis of semi-conductive nanofibers for the stimulation of osteoblasts,* FEM analysis, chemical synthesis and cell culture experiments, September 2018

Acknowledgements

Firstly, I would like to thank my supervisors in Italy – Professor Gianluca Ciardelli and Chiara Tonda Turo – and in the host institution – Dr. Annina Steinbach, Dr. Thomas Winkler, and Dr. Derrick Roberts – for the possibility of working on such an interesting project. Their expertise, their passion and their precious advice were fundamental in this gratifying research program.

I would also like to thank Dr. Cristopher Spicer, Dr. Cristopher Wood, and Mrs. Lisa Nadal for their time and their precious explanations and discussions in the chemical synthesis lab: the introduction to chemistry I received has been an extremely valuable experience.

I would like to acknowledge Professor Molly Stevens, who gave me the opportunity to explore the fields of biology, chemistry and tissue engineering; working in her lab has been an honor.

Many thanks to all the members of the Stevens Group and the MBB department for all the conversations on science, the career advice and the engaging discussions during the breaks.

Most importantly, I would like to thank my family and my friends for all the encouragement and the support I received during these years; their help has been invaluable.

ABSTRACT

This work describes the Master's Thesis project carried out at the Karolinska Institute. The goal was to study the response of osteoblasts to electrical stimulation delivered through semi-conductive nanofibers. A finite element method (FEM) analysis of the system was performed, with the goal of determining the profile of the electric field in the cytoplasm and in the cell membrane. The fibers were then synthesized following the method laid out by Dr. Christopher Spicer [1]. Finally, an experimental set-up was developed, in order to stimulate cells inside a cell culture 12-well plate. The cells' response to electric fields delivered through the synthesized nanofibers was analyzed.

Obiettivo di questo studio era l'analisi della risposta degli osteoblasti a stimoli elettrici prodotti da nanofibre semiconduttive.
Dapprima sono stati studiati i campi elettrici attraverso il metodo degli elementi finiti, il che ha permesso di determinare il comportamento del campo all'interno della membrana cellulare e del citoplasma. In seguito, allo scopo di riprodurre con un esperimento i risultati ottenuti, è stata effettuata una sintesi chimica delle nanofibre, seguendo il metodo messo a punto da Spicer e colleghi [1]. Infine, è stato realizzato un set-up sperimentale che ha permesso di utilizzare le nanofibre sintetizzate per stimolare gli osteoblasti. La risposta delle cellule è stata analizzata con la misura di proliferazione e mineralizzazione della matrice extracellulare.

L'objectif de cette étude était d'analyser la réponse des ostéoblastes à des stimulations électriques produites par des nanofibres semi conductrices.
D'abord on a étudié les champs électriques par la méthode des éléments finis, ce qui a permis de déterminer le comportement du champ à l'intérieur de la membrane cellulaire et du cytoplasme. Ensuite, dans le but de reproduire par expérimentation les résultats obtenus, on a effectué une synthèse chimique des nanofibres, selon la méthode mise au point par Spicer et collab. [1]. Enfin, on a réalisé un système expérimental qui a permis d'utiliser les nanofibres synthésées pour stimuler les ostéoblastes. La réponse des cellules a été analysée par la mesure de la prolifération et de la minéralisation de la matrice extracellulaire.

CONTENTS

I INTRODUCTION 1

1 NANOSTRUCTURES FOR ELECTRICAL STIMULATION IN BONE TISSUE ENGINEERING 3

II SIMULATIONS 5

2 FINITE ELEMENT METHOD ANALYSIS 7
- 2.1 Modeling electric field - cell interaction . . . 7
- 2.2 A cell subjected to an electric field . . . 8
  - 2.2.1 COMSOL implementation . . . 8
  - 2.2.2 Results and discussion . . . 10
- 2.3 The electric double layer . . . 11
  - 2.3.1 Theoretical background . . . 11
  - 2.3.2 FEM simulation . . . 11
  - 2.3.3 COMSOL implementation . . . 12
  - 2.3.4 Results and discussion . . . 15
  - 2.3.5 Potential applications for the fibers . . . 18
- 2.4 Frequency study . . . 19
  - 2.4.1 COMSOL implementation . . . 20
  - 2.4.2 Results and discussion . . . 21
- 2.5 Conclusions . . . 24

III EXPERIMENTAL WORK 27

3 CHEMICAL SYNTHESIS 29
- 3.1 Techniques employed . . . 29
  - 3.1.1 Palladium catalysed cross-coupling reactions . . . 29
  - 3.1.2 Column Chromatography . . . 30
  - 3.1.3 Nuclear Magnetic Resonance spectroscopy . . . 31
- 3.2 The Material . . . 31
- 3.3 Di-capped Oligo-EDOT derivative . . . 32
- 3.4 Focus on the reactions . . . 33
- 3.5 Materials and methods . . . 34
- 3.6 Conclusions . . . 37

4 CELL CULTURE EXPERIMENTS 39
- 4.1 Introduction to the cells and the methods employed . . . 39
  - 4.1.1 Stem Cells and Progenitor Cells . . . 39
  - 4.1.2 Osteoblasts and MC3T3-E1 cells . . . 39
  - 4.1.3 Electrical Stimulation in bone Tissue Engineering 40
- 4.2 Materials and methods . . . 42
  - 4.2.1 The CyQuant Proliferation Assay . . . 42
  - 4.2.2 The Alizarin Red Quantification Assay . . . 43
- 4.3 Optimization of the experimental set-up . . . 44
  - 4.3.1 Platinum wires underneath the lid . . . 44

4.3.2 Platinum wires through the lid 45
4.3.3 Needles through the lateral walls 46
4.3.4 Test of the final experimental set-up 47
4.4 Cell culture on Oligo-EDOTs 47
4.4.1 Materials and methods 47
4.4.2 Results 48
4.4.3 Discussion 49
4.5 Conclusions 50

BIBLIOGRAPHY 55

LIST OF FIGURES

Figure 1 The geometry of the set-up. The front part of the wall was made invisible in order to visualize the cell inside. The values of the geometrical parameters are reported in Table 2. 8

Figure 2 The electric field values in the membrane, according to this first preliminary study 10

Figure 3 The electric field in the membrane of the cell, resting on top of the grounded electrode . . . 10

Figure 4 The dimentionless charge density profile between the two electrodes. The three different curves represent three values of the parameter $\epsilon_D = \frac{\lambda_D}{L}$. This emphasizes the differences that emerge when changing the distance between electrodes. In order to represent systems of different lengths on the same graph, the variable x/L is used: referring to Table 3, since x varies between 0 and L, this new variable spans between 0 and 1, independently of L. The plotted quantity has been made dimentionless dividing by the constant value c_{ref}. 14

Figure 5 The charge distribution profile and its analytical fit using equation 11. 15

Figure 6 Dimentionless charge concentration around a fiber, under the assumption that the study conducted by Bayly and collegues [17] can be extended to a two-dimensional case. 16

Figure 7 COMSOL model of a portion of a cell - the uppermost region - placed on top of an array of equally spaced fibers. 17

Figure 8 The electric field generated using fibers, plotted inside and outside the cell 17

Figure 9 The electric field induced by the fibers in the membrane. 18

Figure 10 The voltage profile across the medium. The distance between the two electrodes is 100 µm. At low frequencies the voltage is constant in the medium and drops only in the region in contact with the electrodes. When the frequency becomes large enough, the impedance of the virtual capacitor drops and the voltage varies linearly with the distance from the fibers. Values are plotted when the phase of the field is 0°. 21
Figure 11 The voltage profile across the medium. As expected, there is a larger voltage drop in the region occupied by the medium at higher frequencies. Values are plotted when the phase of the field is 0°. 22
Figure 12 The electric field profile found in the medium. For high frequencies, the electric field intensity varies greatly with the distance from the fibers: different regions of the cell experience significantly diverse fields. Values are plotted when the phase of the field is 0°. The dots represent the point in which the field was computed by COMSOL (the line is an interpolation of those points). 23
Figure 13 The geometry considered: a spherical cell is resting on top of equally spaced nanofibers, in order to receive AC stimulation. 24
Figure 14 The electric field inside the membrane as a function of the frequency. At low frequencies, the electric field is very small, because the voltage is more or less constant after the double layer (a). It increases with frequency (b) and at very high frequencies (c-d) there is a significant spatial variation of the electric field inside the membrane, with the periodicity of the fibers appearing in the intensity profile. Values are plotted when the phase of the stimulus is 0°. The shape of the membrane has been distorted for improved visibility. Fibers (not shown) can be found at x=0 and at x= −400 nm. 25

Figure 15 The electric field inside the cytoplasm of a spherical cell on top of an array of fibers at different frequencies. Its intensity increases with the frequency: above 10 MHz, the field can fully penetrate inside the cytoplasm. At very high frequencies (c-d), the intensity profile follows the same spatial periodicity of the fibers. Values are plotted when the phase of the stimulus is 0°. 26
Figure 16 The process involved in palladium-catalysed cross coupling reactions. Palladium oxidation state is 0 after reductive elimination and rises to 2 with the oxidative addition. 30
Figure 17 The glyoxylated EDOT: the oxygen atoms pull the electrons away and make the system unreactive 33
Figure 18 The delocalization that makes the amine group unreactive. The R group can represent any hydrocarbon fragment. 33
Figure 19 The first reaction of the process, during which one of the amine groups becomes protected by the tert-butyloxycarbonyl group. 34
Figure 20 The glyoxylation of the EDOT 34
Figure 21 The mono-protected diamine is bonded to the glyoxylated EDOT 35
Figure 22 The bromination of the EDOT derivative. . . . 35
Figure 23 The direct arylation that allows to form the chain of EDOTs 36
Figure 24 The biogenesis of osteoblasts, according to Rutkovskiy et al. [59]. Depending on which gene is expressed, MSCs can directly become osteoblasts or differentiate into osteo-chondro progenitors (they can also undertake different paths if other transcription factors are expressed: those paths are not shown in the scheme). If pre-osteoblasts stem directly from MSCs, they will give rise to skull and clavicle tissues; if they originate from osteo-chondro progenitors, they will form the axial skeleton and the bones of the extremities. Hypertrophic chondrocytes regulate the differentiation of perichondral cells, but in some cases, they can even become pre-osteoblasts. 41

Figure 25 Schematic of the connections. The coloured lines represent wires, the circles are representing the crocodile connectors and the thin black lines are the needles, the final element in the chain from the voltage generator to the ITO glass. 44
Figure 26 A platinum wire passing underneath the lid of a 12-well plate 45
Figure 27 Platinum wire passing through the lid. It would be possible to minimize the wire consumption even more by avoiding the arch, but the number of crocodile connectors is limited, and it is not possible to connect all the samples individually. 46
Figure 28 A needle passing through two walls of the plate. The structure is stable and the needle is securely in place. 47
Figure 29 The needle in Figure b) cannot move further to the left because segment s is longer than the distance between point H and the contact point G in Figure a). At this point the needle cannot slide anymore and the system is stable. 48
Figure 30 The counter electrode, represented by the steel needle, reaches the inside of the well passing through a hole in the lid 49
Figure 31 The results of the mineralization assay (first two columns on the left) of the experiment described in subsection 4.3.4. Samples stimulated by ITO glass are in the corners, cells with no glass in the central row and cells on unstimulated ITO glass are in the remaining wells (A2 and C2) 50
Figure 32 The well plate for the experiment of Section 4.4, after 10 d of electrical stimulation 51
Figure 33 The results of Alizarin Red assay on the EDOT-based material. The mineral crystals (in dark colour) are large and expanded. 52
Figure 34 The result of Alizarin Red assay on ITO glass. The crystals of minerals are tiny and the mineralization appears more scarce than in Figure 33. 52

Figure 35 Absorbance of solubilized Alizarin Red mineral stains from MC3T3-E1 cells cultured for 10 d on EDOT-based material on ITO glass (blue), on ITO glass only (green) and on cell culture plastic as a control (orange). The error bars represent the standard deviation. 53

Figure 36 Fluorescence of the cell lysate bound to the CyQuant GR dye. The lysate was obtained from MC3T3-E1 cells stimulated for 10 d using EDOT-based material on ITO glass (blue) and ITO glass only (green). The error bars represent the standard deviation. 53

LIST OF TABLES

Table 1 List of the variables and parameters used in this section, together with their physical meaning. 9

Table 2 List of the parameters used in this study. The values were taken from [11], where an analogous study was performed. 9

Table 3 List of the variables and parameters used in this section, together with their physical meaning 12

Table 4 List of the variables and parameters used in this section, together with their physical meaning. 20

ACRONYMS

BOC2O Di-tert-butyl dicarbonate

DCM Dichloromethane

DMF Dimethylformamide

DPBS Dulbecco's Phosphate Buffer Saline

ECM Extra-cellular matrix

EDTA Ethylenediaminetetraacetic acid

FBS Fetal Bovine Serum

FEM Finite Element Method

MSC Mesenchymal stromal cell

NMR Nuclear Magnetic Resonance

PBS Phosphate Buffer Saline

PC Progenitor Cell

PEDOT Poly(3,4-ethylenedioxythiophene)

PEG Polyethylene glycol

PFA Paraformaldehyde

RF Radio Frequency

SC Stem Cell

TF Transcription Factor

Part I

INTRODUCTION

1

NANOSTRUCTURES FOR ELECTRICAL STIMULATION IN BONE TISSUE ENGINEERING

Over the last years, the use of nanotechnologies and nanomaterials in the fields of biology and medicine has been increasing; the applications are varied, ranging from drug delivery to tissue engineering [2]. The size of nanostructures makes them ideal for a plethora of different functions such as labeling biomolecules or delivering a drug in response to a specific stimulus [3].
The study of biological tissues and their regeneration highlighted the importance of the extra-cellular matrix (ECM), a complex network that occupies the extracellular space and guides the behavior of cells [3]. Recent progress in nanotechnology and nanofabrication techniques enable the creation of biomimetic structures, closely mimicking the ECM [4]. Nanostructures can thus play a fundamental role in the field of tissue engineering and regeneration.

Electric fields have the potential to greatly improve tissue restoration. These stimuli can affect migration, proliferation, and differentiation of cells [5]. In particular, the bone tissue can greatly benefit from an electrical stimulus: *in vitro* experiments showed that osteogenic differentiation increases, accompanied by an enhancement of ECM mineralization and cell proliferation [6, 7, 8]. *In vivo* studies demonstrated that bone defects and fractures heal faster [6].

The work presented in this thesis deals with the electrical stimulation provided to osteoblasts by means of nanostructures (nanofibers). At first, a Finite Element Method (FEM) analysis is carried out to determine the profile of the electric field generated by such structures when in contact with cells and their culture media (Chapter 2). Subsequently, polymer that the nanofibers are based on is synthesized using an oligo-EDOT-based material. The aim of this second step is to realize a material that is characterized by a defined chemical structure, leading to well-defined physicochemical properties (Chapter 3). The last part of the work centers on the development of an experimental set-up to provide cells with electrical stimulation inside a common 12-well plate. The set-up is then used to test the effects of an electrical stimulus provided by the oligo-EDOT-based nanofibers. The proliferation of cells and the mineralization of the ECM are tested and compared to control experiments (stimulus provided by a flat electrode and unstimulated cells) (Chapter 4).

Part II

SIMULATIONS

2 FINITE ELEMENT METHOD ANALYSIS

This chapter collects the results and the discussion on the simulation work carried out using COMSOL Multiphysics. This software is based on the Finite Element Method (FEM), that is often employed when dealing with complex analytical problems. When using the FEM approach, the system under study is subdivided into small regions, in which - by assumption - each physical quantity varies linearly [9]. By imposing continuity wherever two different regions meet, a large system of equations is obtained. Starting from the user-defined boundary conditions, COMSOL Multiphysics lets the quantities of interest vary in each region until it finds the configuration that minimizes the total energy [10]. This configuration is assumed to be the (approximate) numerical solution to the problem considered.

The goal of this section is to visualize and comprehend the behavior of the electric field generated by nanofibers in contact with the cytoplasm and the cell membrane. The final objective is to obtain an accurate modeling of the geometry of the nanofibers, considering the electric double layer that forms at the electrode-electrolyte interface. To this end, simulations have been broken down in several simpler steps, eventually integrated into one comprehensive study.

2.1 MODELING ELECTRIC FIELD - CELL INTERACTION

The interaction between a cell and an electric field is a complex mechanism that requires an accurate modeling [11]. Several theoretical models have been put forward, where the cell is approximated by spherical, cylindrical and ellipsoidal shells for which Laplace's equation is solved [12, 13]. A variety of FEM analyses have also been carried out, in order to obtain numerical solutions for more complex and realistic systems: in particular, Taghian and colleagues have analyzed the response of a cell to electric fields with various different frequencies, taking into account the role played by the extracellular matrix (ECM) [11]. In their paper, Taghian and co-workers have considered electrodes that are isolated from the medium: the electric field is coupled to the cell capacitively, and electrochemical processes are not examined. The work presented in this Chapter starts from their analysis, but then considers electrodes that are placed in direct contact with cells and culture medium: the formation of a double layer of charges is studied in detail, comparing the results obtained using different physical models.

2.2 A CELL SUBJECTED TO AN ELECTRIC FIELD

As the first step in this study, a simplified version of the general model is considered: a spherical cell, immersed in the culture media, is resting on top of a grounded circular electrode (reference). 100 µm above, another circular electrode is placed, fixed at 1 V. The goal of the study is it obtain the electric field distribution between the two electrodes, and in particular in the cytoplasm and in the cell membrane. The 3D representation of the geometry under study is shown in Figure 1.

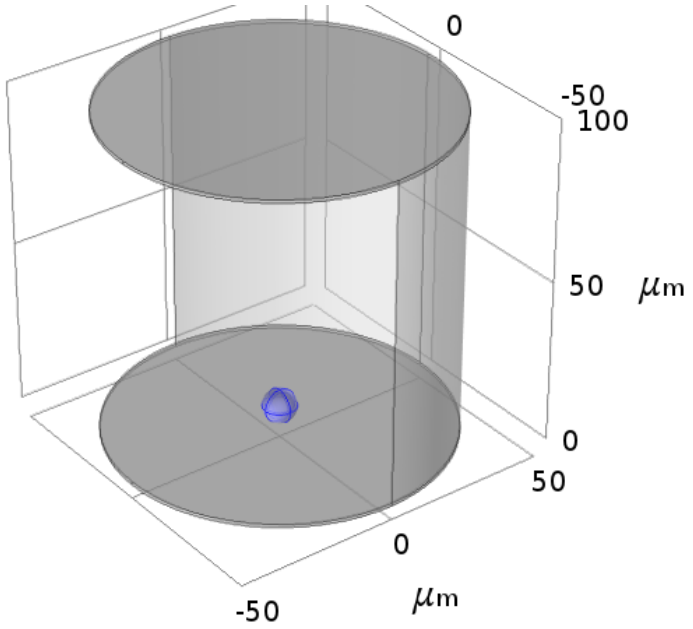

Figure 1: The geometry of the set-up. The front part of the wall was made invisible in order to visualize the cell inside. The values of the geometrical parameters are reported in Table 2.

2.2.1 *COMSOL implementation*

A series of variables is used in this subsection: they are listed in Table 1. The problem is described by two conditions: the voltage of the two electrodes is fixed and there are no external sources of electric field - it is an isolated system. This latter condition is implemented by COMSOL by default, through equation 1 [14].

$$\vec{n} \cdot \vec{D} = 0 \tag{1}$$

Table 1: List of the variables and parameters used in this section, together with their physical meaning.

$\vec{E}$	electric field
V	voltage
ϵ_0	absolute permittivity
ϵ_r	relative permittivity
$\vec{D}$	electric displacement field
ρ_V	charge density
$\vec{n}$	unitary vector normal to a surface

Table 2: List of the parameters used in this study. The values were taken from [11], where an analogous study was performed.

PHYSICAL OR GEOMETRICAL QUANTITY	VALUE
Cell radius	$5\,\mu m$
Membrane thickness	$5\,nm$
Electrode radius	$50\,\mu m$
ϵ_r, culture media	80
ϵ_r, cytoplasm	80
ϵ_r, membrane	11.3

In order to put the boundary conditions in relation with the quantity of interest (the electric field), two equations are sufficient:

$$\vec{E} = -\nabla V \tag{2}$$

$$\epsilon_r \epsilon_0 \vec{E} = \vec{D} \tag{3}$$

where 2 is immediately obtained considering that the electrostatic field is conservative and 3 is the definition of the electric displacement field.

The cell membrane is implemented as the difference between two spheres, with radii differing by $5\,nm$. Because equations 2 and 3 are employed, the only physical parameter that is important in the study is the relative permittivity of the various materials. According to Taghian and colleagues [11], the cytoplasm and the cell medium have the same ϵ_r; for what concerns this study the cell is simply a thin hollow lipid membrane.
The values of the geometrical and physical parameters used are listed in Table 2.

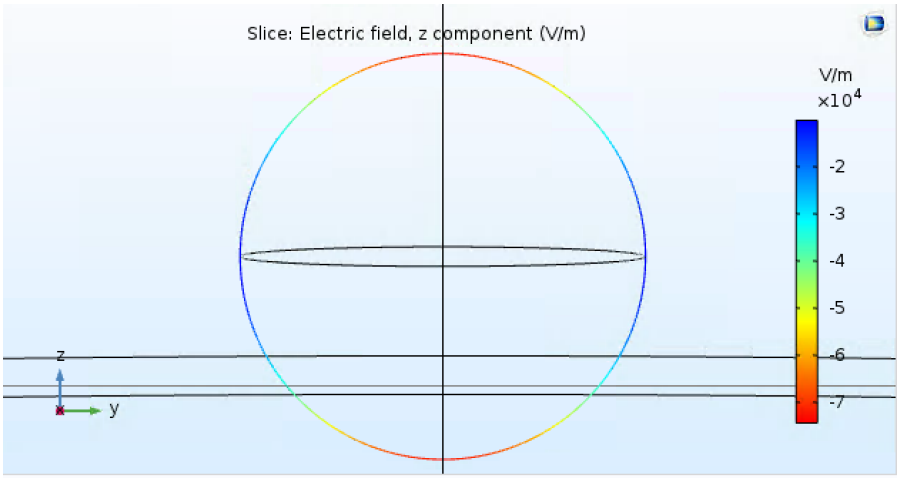

Figure 2: The electric field values in the membrane, according to this first preliminary study

2.2.2 *Results and discussion*

The electric field distribution obtained is in accordance with the results of Taghian and colleagues [11]. The field is maximum in contact with the electrode and it decreases moving away from it until the horizontal symmetry plane; then it increases again forming a symmetrical profile, with the maximum of the field on the upper apex. This is represented in Figure 2 and 3.

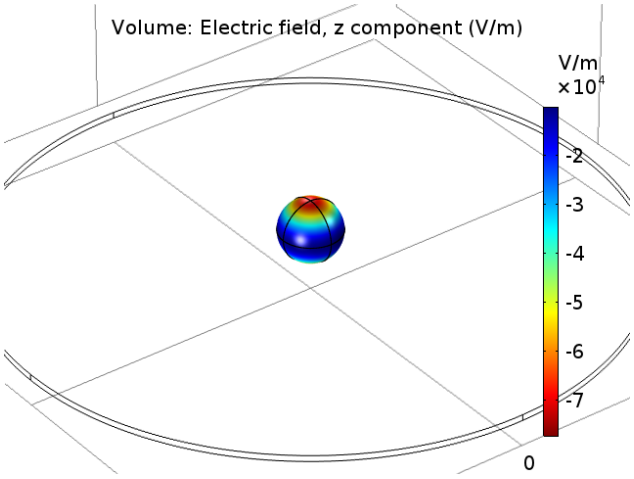

Figure 3: The electric field in the membrane of the cell, resting on top of the grounded electrode

2.3 THE ELECTRIC DOUBLE LAYER

2.3.1 *Theoretical background*

When a charged electrode is immersed in a liquid, a layer of ions forms at the interface, profoundly influencing the intensity and the profile of the electric field [15]. There are several models describing the behavior of the particles in the vicinity of the electrode surface:

- *The Helmoltz model*: It works under the assumption that no electron transfer occurs at the interface. Because the electrode is charged, ions close to the surface will redistribute: the ones that are attracted by the electric field will accumulate close to the interface, balancing the charge present on the electrode. Another assumption is made: the distance of approach is limited to the solvation sphere around each ion. The result is a double layer of charges, separated by a distance: this is electrically equivalent to the description of a capacitor [15].
- *The Gouy-Chapman model*: It was put forward in order to address some of the limitations of Helmoltz's model. It considers the thermal motion of ions and uses Maxwell-Boltzmann statistics (accounting for the electrostatic field) in order to determine the charge distribution. In this way, the electric potential follows an exponential decay: this corresponds to the description of a diffusive layer [16].
- *The Stern model*: This model is a combination of the two previous models. It considers a fixed layer of charges at the interface with the electrode, followed by a region where the ion distribution is governed by drift (under the electrostatic field) and diffusion [15].

The Stern model is the most complicated approach, but also the one able to better describe the double layer. For this reason, it is the model used in this Section. In Section 2.4, where the effect of an alternating field are analyzed, the Helmoltz model is considered and the two approaches are compared.

2.3.2 *FEM simulation*

Implementing an electric double layer in COMSOL can be a complex task: the problem is highly non-linear. A first study is conducted with the goal of reproducing the results obtained by Bayly and colleagues [17], to verify if the implementation is correct. This study considers two electrodes placed at a distance L: the concentration of ions and the voltage profiles between those two electrodes are obtained combining the Nernst-Planck equation with Poisson's equation.

As a step towards the actual experiment set-up, one metallic flat electrode is then substituted with polymeric cylindrical fibers: with a mathematical transformation (see 2.3.3), the new charge distribution is extrapolated from the previous study.
Finally, the effects of this charge distribution on a cell are analyzed, with particular attention to the electric field across the membrane.
The meaning of all the symbols used in this section are summarized in Table 3.

Table 3: List of the variables and parameters used in this section, together with their physical meaning

ρ_s	surface charge density
ϕ_M	electrode voltage
ϕ	voltage variable
λ_S	Stern layer thickness
$\vec{D_1}$, $\vec{D_2}$	electric displacement vectors
$\vec{n}$	unit vector orthognal to the surface of contact
D_i	diffusion coefficient of species i
c_i, $i = +, -$	concentration of species i
u_i	mobility of species i
z_i	electric charge of species i
F	Faraday's constant
c_{ref}	ions concentration in the bulk
$\vec{N_i}$	flux of species i
k_a, k_c	anodic and cathodic rate constant
c_M, c_p	species activity (metal or positive ions)
α_a, α_c	anodic and cathodic transfer coefficient
T	temperature
R	gas constant
λ_D	Debye length
L	distance between electrodes
x	space variable (varying between 0 and L)
r	radius of the fiber
α, β, γ, k	numerical parameters used to optimize the quality of the fit

2.3.3 *COMSOL implementation*

Following the study of Bazant et al.[17], the Stern model is implemented. In COMSOL, this is done through two different steps: a first

set of equations and boundary conditions represents the fixed layer, and a second one the diffusive region.

The fixed layer is described by equations 4 and 5:

$$\rho_s = \epsilon_0 \frac{\phi_M - \phi}{\lambda_S} \tag{4}$$

$$\rho_s = \vec{n} \cdot \left(\vec{D_1} - \vec{D_2}\right) \tag{5}$$

Equation 5 is the boundary condition for the electric displacement field at the interface between two materials [18]. Equation 4 is chosen so that by substituting 4 in 5, one gets a linear relationship between the voltage (ϕ) and the distance from the electrode (in the region where the fixed charge layer is present). This behavior is typical of capacitors.

The Nernst-Planck equation 6 describes the transport of molecules subjected to an electric field (drift) and to a gradient of concentration (diffusion):

$$-D_i \nabla c_i - u_i z_i F c_i \nabla \phi = \vec{N_i} \tag{6}$$

Where the fibers or the counter electrode are in contact with the liquid, deposition and dissolution of ions occur [17]: in these regions, $|\vec{N_i}|$ from equation 6 is equal to the reaction rate given by Arrhenius equation 7:

$$r = k_c c_p e^{-\frac{\alpha_c F \phi_\Delta}{RT}} - k_a c_M e^{\frac{\alpha_a F \phi_\Delta}{RT}} \tag{7}$$

where $\phi_\Delta = \phi_M - \phi$. Bazant and colleagues considered metal electrodes [17]; because anions hardly adsorb on metal surfaces, the reaction rate for the negative species is set to zero:

$$\vec{N_-} = 0 \tag{8}$$

In order to compare the results with the findings of Bazant and colleagues [17], the current experienced by one of the electrodes is set to 90% of the faradaic limiting current.

$$i_{electrode} = 0.9 \cdot i_{lim} = 0.9 \cdot \frac{4FD_+c_0}{L} \tag{9}$$

During the simulation, the software computes the voltage necessary to sustain this condition. The other electrode is simply grounded.
The voltage in each point in space is obtained by means of Poisson's equation 10:

$$\nabla\left(-\epsilon \nabla \phi\right) = \rho = F\left(c_+ - c_-\right) \tag{10}$$

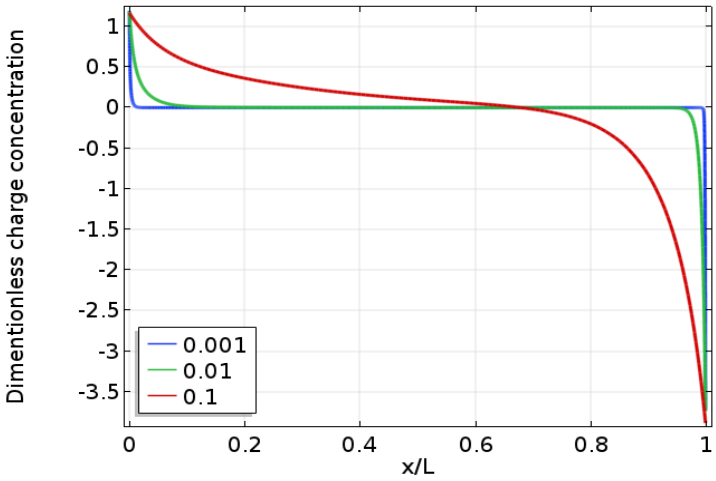

Figure 4: The dimentionless charge density profile between the two electrodes. The three different curves represent three values of the parameter $\epsilon_D = \frac{\lambda_D}{L}$. This emphasizes the differences that emerge when changing the distance between electrodes. In order to represent systems of different lengths on the same graph, the variable x/L is used: referring to Table 3, since x varies between 0 and L, this new variable spans between 0 and 1, independently of L. The plotted quantity has been made dimentionless dividing by the constant value c_{ref}.

Finally, the variables ρ and ϕ that appear in different equations are coupled using the Multiphysics interface. The result of this study is represented in Figure 4 and further analysed in subsection 2.3.4.

The expected behavior – because of Maxwell-Boltzmann statistics – is an exponential decay. However, while a fit with an exponential function provides indeed a good result, the best outcome is obtained using 11. The cause of this behavior is probably the mesh, which cannot be made infinitely fine.

$$y = \alpha_0 + \frac{\beta}{1 + \gamma x^k} \tag{11}$$

With the simple transformation:

$$x \to \sqrt{x^2 + y^2} - r \tag{12}$$

the function depicted in Figure 6 is obtained. It is defined just for $\sqrt{x^2 + y^2} > r$ and it is the two-dimensional radially symmetric extension of the results obtained by Bayly and collegues [17].

The geometry of Figure 7 is then considered: fibers are made out of a conductive material (relative permittivity equal to 1), while the cell is modeled as a hollow sphere with relative permittivity equal to 11.3 as in subsection 2.2.1. From the physical point of view, the study is completely analogous to the first one of this Chapter. For what concerns the boundary conditions, the fibers are grounded and the zero

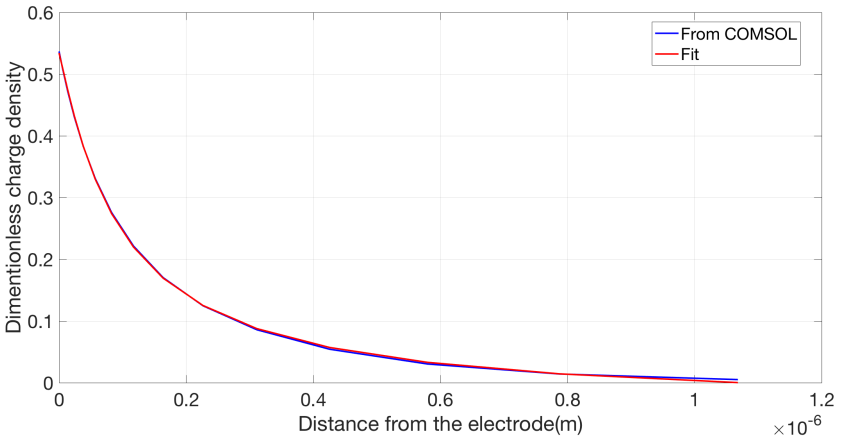

Figure 5: The charge distribution profile and its analytical fit using equation 11.

charge condition ($\vec{n} \cdot \vec{D} = 0$) is applied on the uppermost boundary, to force bulk electroneutrality (see section 2.3.4). The whole geometry is divided into five equal sections, centered around the fibers, and each one of these sections hosts the space charge density of Figure 6 (with a factor $2F \cdot c_{ref}$ in order to have a quantity expressed in C/m^3).

2.3.4 *Results and discussion*

According to this second study, if the distance between the two electrodes is very short (comparable with the Debye length), the system reaches electroneutrality in a single point. However, when the two electrodes are placed further apart, two effects occur:

- The areas close to the electrode, where the effects of the double layer can be appreciated, become negligible compared to the dimension of the system: the macroscopic limit is approached, and bulk electroneutrality can be assumed ($|c_+ - c_-| \ll c_+ + c_-$) [17].
- Ions can diffuse further away from the electrode: in the vicinity of the electrode, the charge density is higher if the electrodes are more spaced.

Those results are shown in Figure 4 and are in agreement with Bazant et al. [17]. In the case of interest, the distance between the electrodes (1 cm) is much larger than the Debye length (around 100 nm); close to the electrode, the concentration of charges is then expected to be rather high.
If one of the flat metallic electrodes is substituted with a polymeric semi-cylindrical fiber, two important differences arise: anions adsorb on the surface and the charge density profile must become a two-variable function (with radial symmetry). In order to meet these two

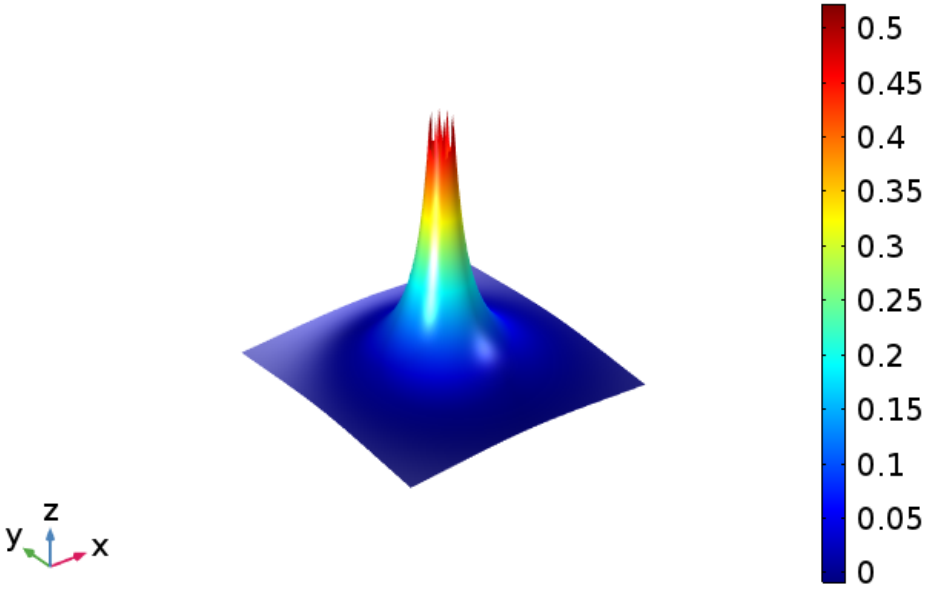

Figure 6: Dimentionless charge concentration around a fiber, under the assumption that the study conducted by Bayly and collegues [17] can be extended to a two-dimensional case.

conditions, as a first step, the results obtained in the previous study are fitted analytically: the outcome is a function that rapidly decays with the distance from the electrodes (represented in Figure 5). The semi-cylindrical fiber is then divided into infinitely small segments dl, so short that they can be approximated as flat. In the direction orthogonal to the segment, the previous study can thus be applied. It is then sufficient to rotate the analytical function (around the y axis, according to Figure 5; an offset is also added to account for the fiber diameter, see 2.3.3 for details) to obtain the charge distribution in each point in space. The result is a two-variable function with radial symmetry. This procedure leads to the distribution of Figure 6.

For the final study of this section, the geometry in Figure 7 was considered. An array of equally spaced fibers is used to stimulate a cell. The charge distribution around each fiber is assumed to be the one in Figure 6; thanks to Poisson's equation, from this distribution it is possible to compute the voltage and the electric field in each point in space.

Given two boundary conditions - the fibers are grounded and far from the electrodes electroneutrality is reached - those two quantities are uniquely determined in this way. The results of this last study are depicted in Figure 8 and Figure 9. The electric field is not constant in the membrane: it is stronger in the regions above the fibers and its

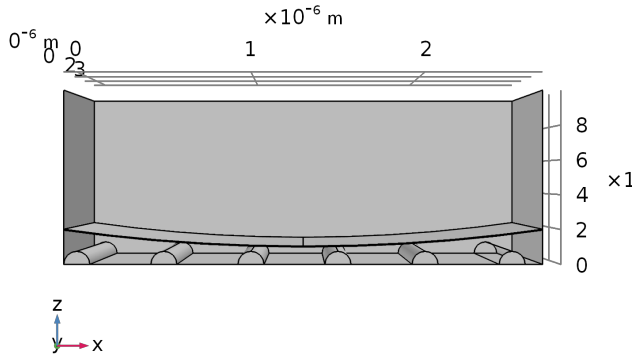

Figure 7: COMSOL model of a portion of a cell - the uppermost region - placed on top of an array of equally spaced fibers.

intensity drops elsewhere. Those results show how these structures spatially confine the electric field, in a region approximately as wide as the fibers themselves. If they are made larger - around 10 µm -, the field can be concentrated around a single cell.

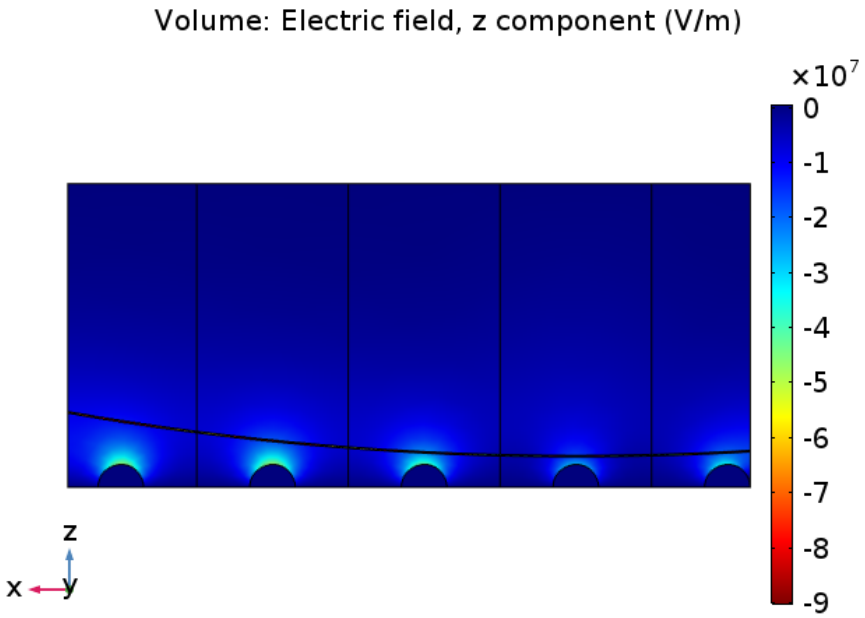

Figure 8: The electric field generated using fibers, plotted inside and outside the cell

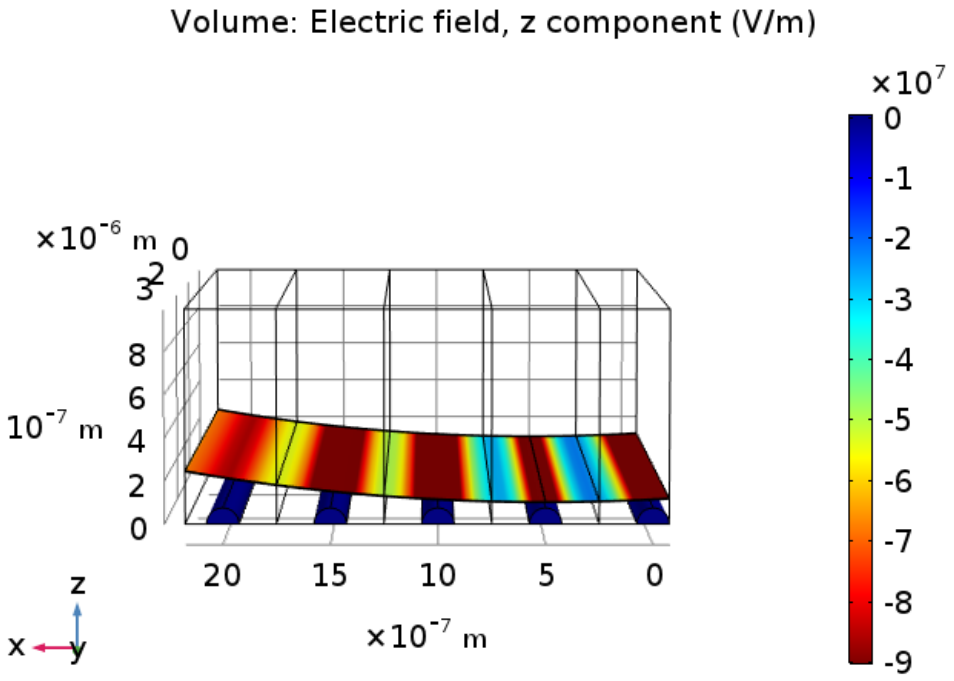

Figure 9: The electric field induced by the fibers in the membrane.

2.3.5 *Potential applications for the fibers*

The possibility to confine the electric field in a very small region (just in a portion of the cell as the results have shown), makes the fibers a promising tool for research in cell biology: some of the potential applications are shown in the following paragraphs.

2.3.5.1 *Integrins*

Integrins are proteins that work as receptors and help cells adhere to the extracellular matrix (ECM). They are involved in all the interactions between the cytoskeleton and the ECM; particularly, they are thought to be capable of inducing localized changes in the cytoplasm in response to external stimuli [19]. Integrins can be redistributed by electric fields [20]: thus, thanks to a localized stimulus it can be possible to affect those proteins, isolate them and better understand their role and function. This can be of interest for cells other than osteoblasts: neurons, for example, grow their axons in response to external signals picked up by integrins [19].

2.3.5.2 *Voltage-dependent channels*

Voltage-dependent channels are constituted by transmembrane proteins; they are of major importance in processes such as action potentials or signal transduction and are activated when the electric

potential in the membrane changes [21, 22]. Because of their nature, it is clear that an electrical stimulus is able to trigger their function: nanofibers can then be employed to investigate action potentials or other electrically-triggered processes by confining the stimulus in a small region and then monitoring its development.

2.3.5.3 *Cell heterogeneity and response amplification*

Cells are extremely heterogeneous structures in space: a single chemical component can trigger different phenotypic responses, depending on its position within the cell [23]. Processes that can be triggered by an electric field (for examples see 2.3.5.2) can in principle benefit from this same property, leading to a variety of different effects depending on which parts of the cell are close to the fibers. Furthermore, it has been proven that when certain stimuli are localized, they trigger an amplified signal response [24].

2.3.5.4 *Membrane clusters*

Membrane clusters are groups of colocalized proteins playing a role in signal detection [23]. DC electric fields are able to trigger the formation of clusters [25]: the nanofibers can then promote the creation of these clusters in specific regions, in order to better understand their role or to investigate the spatial heterogeneity of the cell by stimulating it from different sites.

2.4 FREQUENCY STUDY

Even though low-frequency fields seem to have the greatest impact on osteoblasts [26], pulsed fields are able to promote vascular growth and affect cell signaling [27]. For this reason, it can be of interest to investigate the effects of an electric field that varies over time.
There are different ways to model the electric double layer with varying degrees of complexity; some of them have been presented in subsection 2.3.1. The Stern model is the most accurate one: however, accounting for the diffusion and drift of ions in a time-dependent study is a non-trivial task. It is possible to follow the approach proposed by Brumleve and colleagues [28], by running a series of studies representing the system at different time steps. The process involves the following:

- The flux of ions is computed according to the Nernst-Planck equation (6) at each time step.
- The number of ions entering or leaving each point in space at time $t + 1$ is calculated from the inward or outward flux in that point. This quantity is called Δc_i.

- The concentration in each point at time step $t+1$ is obtained from the concentration at time t by adding Δc_i.

Precision comes at a great computational cost.; however, very satisfactory results can be obtained considering a much simpler model - the Helmoltz one - at a feasible computational effort.

2.4.1 *COMSOL implementation*

A series of variables is used in this section: they are listed in Table 4.

Table 4: List of the variables and parameters used in this section, together with their physical meaning.

$\vec{J}$	total current density
ρ	charge density
σ	conductivity
$\vec{E}$	electric field
$\vec{D}$	electric displacement field
$\vec{P}$	electric polarization

The system is described by two equations: the continuity condition must hold true:

$$\nabla \cdot \vec{J} = -\frac{\partial \rho}{\partial t} \tag{13}$$

The total current density is the sum of the free, the displacement and the polarization currents:

$$\vec{J} = \sigma\vec{E} + \frac{\partial \vec{D}}{\partial t} + \frac{\partial \vec{P}}{\partial t} \tag{14}$$

In COMSOL, a counter electrode is placed on top of a cuboid that represents the culture medium. An array (60 elements) of cylinders models the fibers. The distance between the two electrodes is $100\,\mu m$. $1\,V$ is applied to the counter electrode, while the fibers are grounded. The cell is implemented in the same way presented in subsection 2.2.1: the membrane is the difference between two spheres and the cytoplasm has the same permittivity and conductivity as the medium. The double layer is implemented as a capacitor (*Contact Impedence* node in COMSOL): the value of the capacitance is chosen according to the study of Kisza [29] ($\approx 10\,\mu F\,cm^{-2}$). By default, the zero charge condition is applied to all the boundaries that are not under electrical control. A parametric sweep is then executed, for frequencies ranging from $10\,Hz$ to $500\,MHz$.

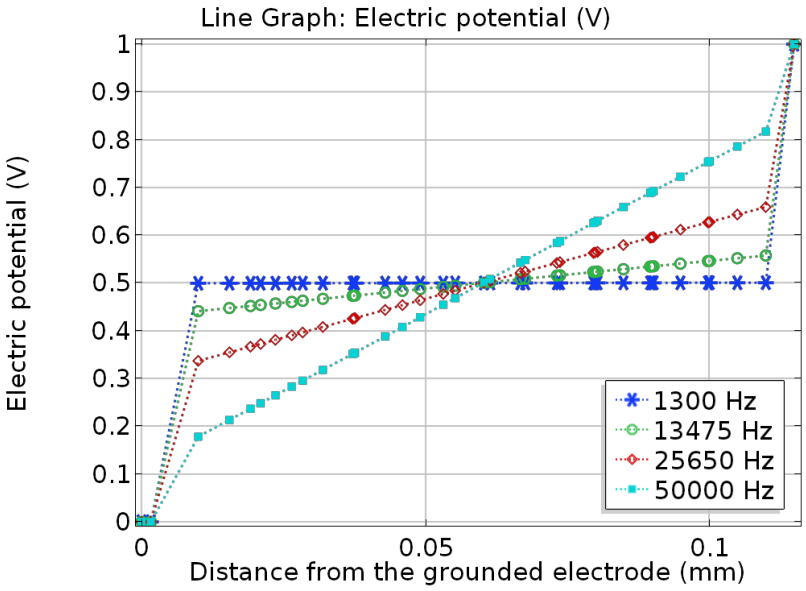

Figure 10: The voltage profile across the medium. The distance between the two electrodes is 100 µm. At low frequencies the voltage is constant in the medium and drops only in the region in contact with the electrodes. When the frequency becomes large enough, the impedance of the virtual capacitor drops and the voltage varies linearly with the distance from the fibers. Values are plotted when the phase of the field is 0°.

2.4.2 *Results and discussion*

According to the Helmoltz model, a double layer of charge is present in contact with the electrode. This layer behaves as a capacitor, from an electrical point of view. By employing a high-frequency field, the impedance of the capacitor becomes small, and the voltage drop across the medium increases. This is exactly what is represented in the results, plotted in Figure 10, where two flat electrodes have been considered.

If one electrode is replaced by fibers, the voltage profile changes to the one represented in Figure 11. Similar considerations apply in this case as well.

As plotted in Figure 10 and 11, at low frequencies the voltage remains almost constant across the whole medium[1]: employing the

1 The small voltage increase in the vicinity of the counter electrode (0.1 mm) of Figure 11 is an artifact of the model. The fiber diameter is much smaller than the counter electrode width, and the mesh follows this difference in dimensions: it is much coarser in the region around 0.1 mm. The last element of the mesh takes charge of the voltage drop on the double layer virtual capacitor: while in the vicinity of the fibers this element is so small that it cannot be appreciated (Figure 11), close to the counter electrode the last piece of the mesh is rather large. It follows that the region where the voltage drops, in the vicinity of the counter electrode, seems to be more spread out in space, instead of being limited to a few nanometers.

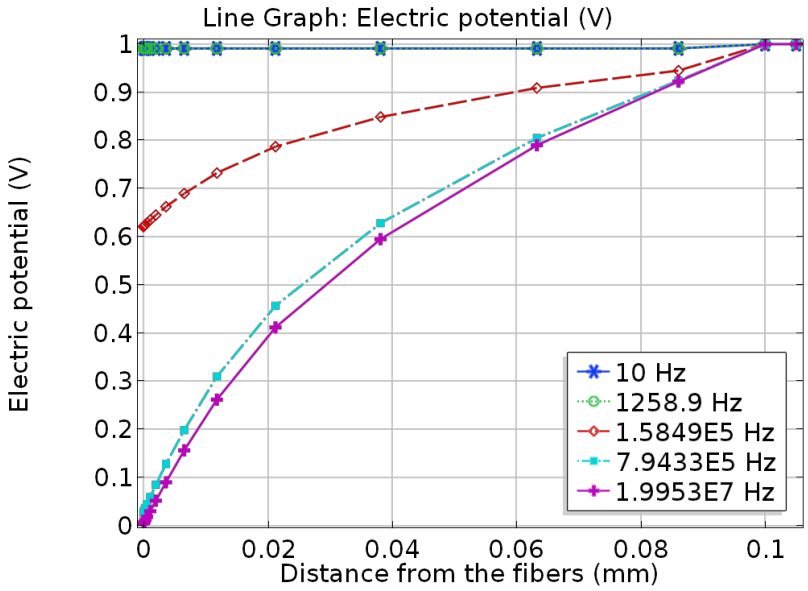

Figure 11: The voltage profile across the medium. As expected, there is a larger voltage drop in the region occupied by the medium at higher frequencies. Values are plotted when the phase of the field is 0°.

Helmoltz model, this is an expected result. In fact, according to the model, the charge of the ions accumulating at the surface exactly balances the charge on the electrode. Furthermore, because ions do not diffuse, electroneutrality is reached immediately after the double layer. Solving Poisson's equation with these two conditions yields that the voltage drops only on the double layer, and remains constant everywhere else.

The results obtained using the Stern model in subsection 2.3.3 are in accordance with this evidence in the limit of a very large distance between the electrodes - when the diffusion region becomes negligible compared to the dimension of the system. For this reason, the results of Figure 11 are a valid approximation for systems that are much larger than their Debye length.

Integrating the voltage in space, according to Equation 2, one gets the graph in Figure 12. When considering higher frequencies (above 100 kHz), i.e. when the impedance offered by the double layer becomes negligible, the results match the first purely electrostatic study (Section 2.2).

A cell on top of the fibers is then considered. It contacts the fibers in one point; the geometry is represented in Figure 13.

The electric field in the cytoplasm and in the membrane have a strong dependence on the frequency. At low frequencies, the voltage drops almost exclusively on the double layer; inside the cytoplasm and across the membrane it remains approximately constant, thus the electric field is very small. At higher frequencies (above 10 MHz)

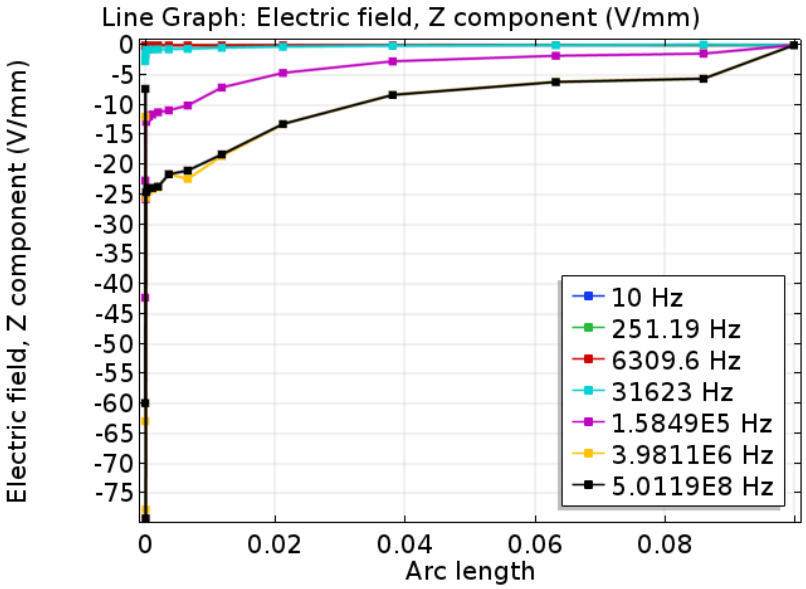

Figure 12: The electric field profile found in the medium. For high frequencies, the electric field intensity varies greatly with the distance from the fibers: different regions of the cell experience significantly diverse fields. Values are plotted when the phase of the field is 0°. The dots represent the point in which the field was computed by COMSOL (the line is an interpolation of those points).

the impedance offered by the double layer drops, and the electric field starts penetrating inside the membrane (Figure 14 b and c). At even higher frequencies, it enters the cytoplasm (Figure 15 d). These results are in accordance to the analytical analysis by Foster [30] and are similar to what Taghian and colleagues have obtained considering the capacitive coupling instead of the double layer [11]. According to Figures 14 and 15, at high frequencies it is again possible to confine the electric field in a region comparable to the dimension of the fibers themselves.

The effects of radio frequency (RF) fields on cells are still under debate; many studies have shown cytotoxic effects caused by high-frequency fields, but results are inconsistent. RF fields are suspected to cause DNA breaks, mutations, reduced proliferation among other issues, besides enhancing the expression of heat shock proteins (released by cells under stressful conditions) [31]. While in general those results are difficult to reproduce, when stimulating cells for tissue engineering it would be safe to avoid the field penetration inside the cytoplasm (the results obtained in this section set a limit at around 10 MHz).

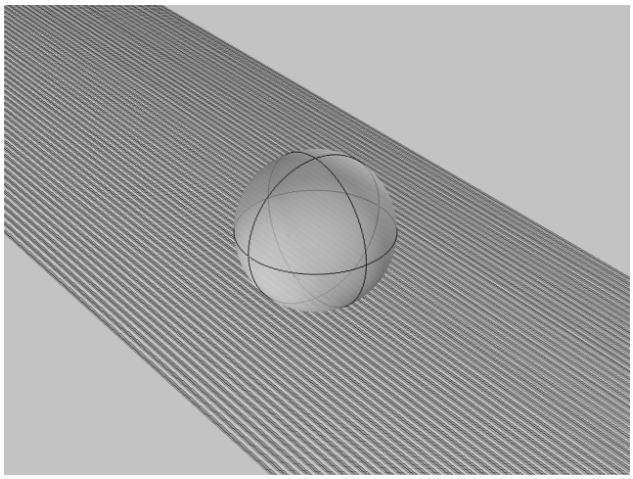

Figure 13: The geometry considered: a spherical cell is resting on top of equally spaced nanofibers, in order to receive AC stimulation.

2.5 CONCLUSIONS

In this Chapter, a FEM analysis of the electric field induced by nanofibers inside the membrane and the cytoplasm of a cell has been presented. The formation of a double layer of charges has been studied, considering the Stern and the Helmoltz models. The diffusion region of ions extends enough to affect the behavior of the electric field where the cell resides. The main finding demonstrates that it is possible to confine the electric field in a region that has the same dimensions as the fiber itself. By properly choosing the diameter, the stimulus can be constrained around a single cell or even in a small portion of it. The nanofibers have potential applications in research in cell biology and can be exploited to grow and manipulate cells that strongly interact with electric fields (neurons, myocytes, and osteoblasts for example). For what concerns the AC study, in the approximation of a very large distance between the two electrodes, the electric field can still be confined in a small region, allowing for the same effects discussed above. However, this confinement appears at very large frequencies, for which the field penetrates inside the cytoplasm. This can be potentially harmful to the cell.

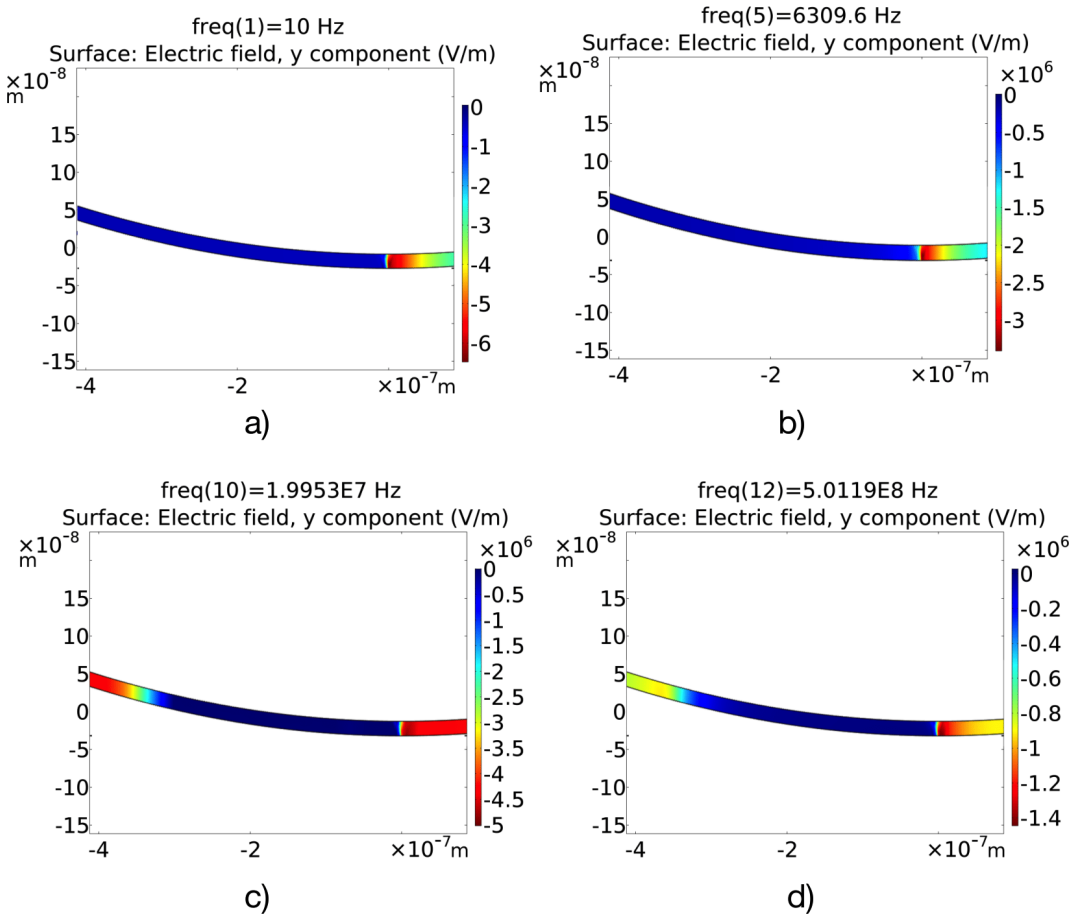

Figure 14: The electric field inside the membrane as a function of the frequency. At low frequencies, the electric field is very small, because the voltage is more or less constant after the double layer (a). It increases with frequency (b) and at very high frequencies (c-d) there is a significant spatial variation of the electric field inside the membrane, with the periodicity of the fibers appearing in the intensity profile. Values are plotted when the phase of the stimulus is 0°. The shape of the membrane has been distorted for improved visibility. Fibers (not shown) can be found at x=0 and at x= −400 nm.

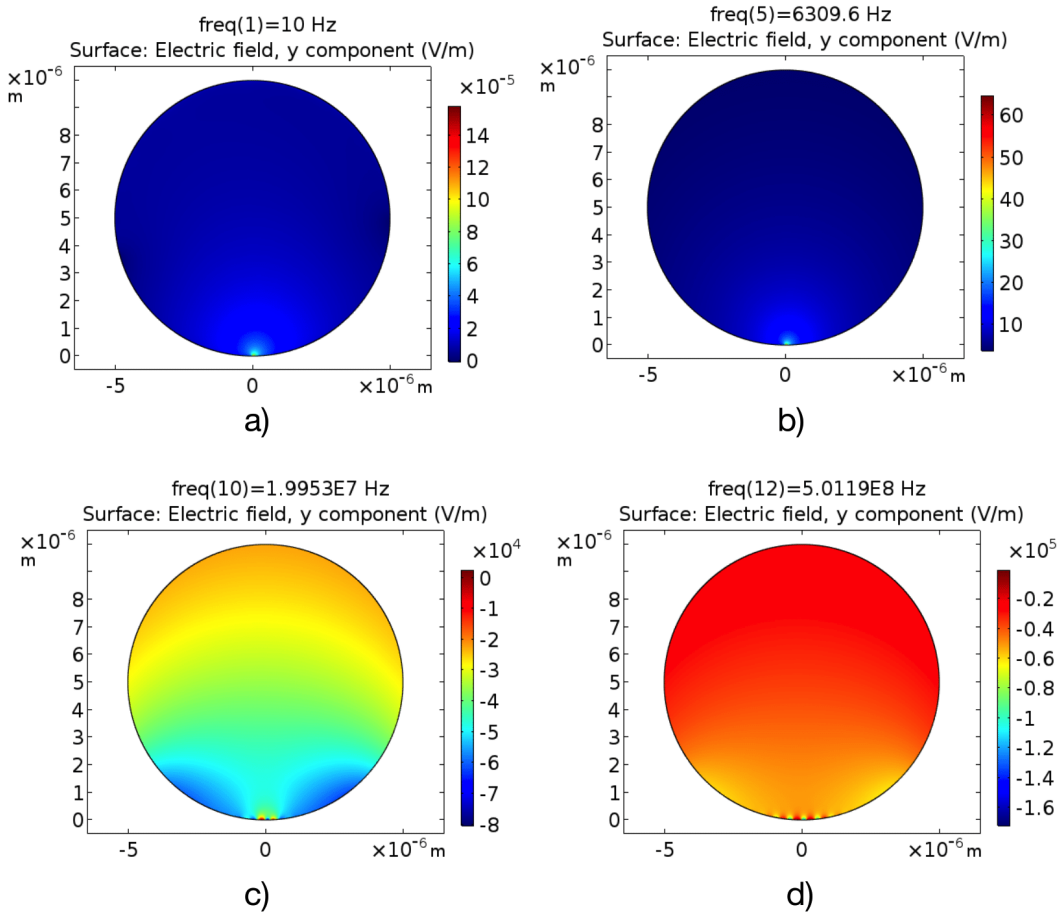

Figure 15: The electric field inside the cytoplasm of a spherical cell on top of an array of fibers at different frequencies. Its intensity increases with the frequency: above 10 MHz, the field can fully penetrate inside the cytoplasm. At very high frequencies (c-d), the intensity profile follows the same spatial periodicity of the fibers. Values are plotted when the phase of the stimulus is 0°.

Part III

EXPERIMENTAL WORK

3

CHEMICAL SYNTHESIS

In this Chapter, the synthesis of a bio-compatible and stable semiconductive material is presented. This material is employed to form the nanofibers whose effects on cells have been modeled in Chapter 2. The nanofibers will then be placed in contact with cells; those experiments are described in Chapter 4.

The rationale behind the choice of the material is presented, together with a discussion on the techniques used for its synthesis and the comparison with other similar works present in literature. Each reaction is then explained in a general overview (3.4) and in experimental detail (3.5).

3.1 TECHNIQUES EMPLOYED

A series of techniques have been employed in order to synthesize, purify and analyze the products of the reactions. While these techniques will be familiar to readers with a background in synthetic chemistry, students from other subject areas–the author included–may require some initial orientation. Consequently, the first section of this Chapter will explain the key experimental methods and techniques used to prepare EDOT-based biomaterials.

3.1.1 *Palladium catalysed cross-coupling reactions*

Palladium catalysis enables or promotes a huge variety of different reactions and for this reason is of fundamental importance in synthetic chemistry. In particular, in this Chapter, palladium catalyzed cross-coupling reactions are exploited: their result is to connect together two different organic fragments, forming carbon-carbon bonds. Palladium catalyzed reactions follow scheme 15.

$$X - R + M - R' \rightarrow R - R' + MX \tag{15}$$

where R and R′ are the organic fragments that undergo coupling, X is usually a halide and M is a metal species. Their general mechanism involves three main steps, summarised in Figure 16:

- Oxidative addition: Pd(0) undergoes oxidation (Pd(II)), inserting between σ bonded atoms.
- Transmetalation: the second organic fragment (R′) exchanges its M-R′ bond for an R′-Pd(II) bond.

- Reductive elimination: opposite to oxidative addition, a σ bond is formed between the two organic fragments, while palladium is reduced and dissociates from the compound. At this point, the process can be repeated.

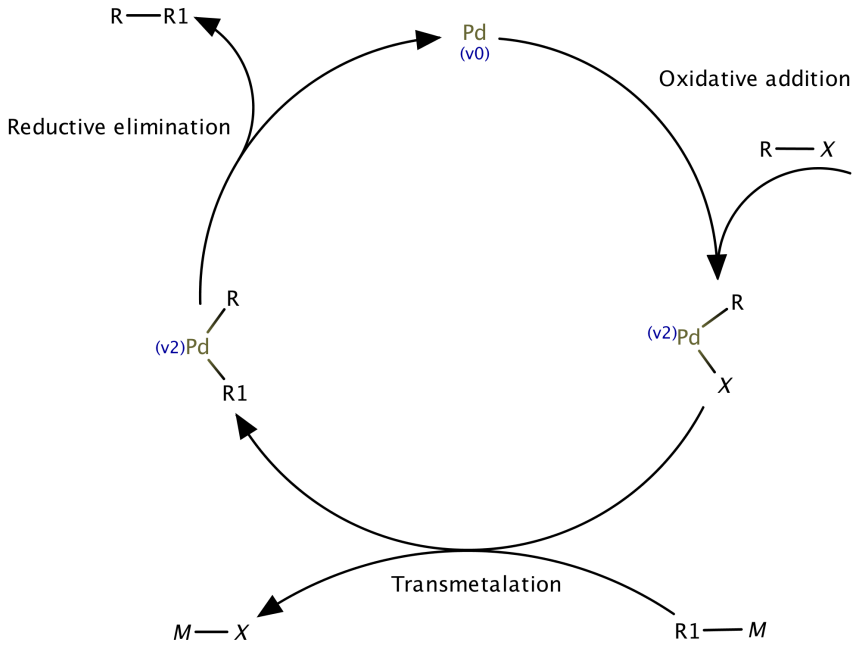

Figure 16: The process involved in palladium-catalysed cross coupling reactions. Palladium oxidation state is 0 after reductive elimination and rises to 2 with the oxidative addition.

Different cross-coupling reactions involve different metals or nucleophilic species. For example, Stille reactions are palladium-catalyzed cross couplings between allyl, alkenyl or aryl groups, where X is a halide and M is tin [32].
For catalysis, palladium complex are employed: the ligands attached to the palladium centre can drastically effect the suitability of the catalyst for different reaction types and the rate of catalytic turnover. For instance, the ease of oxidative addition or reductive elimination can be tuned by changing the electron density around the palladium atom [33].

3.1.2 *Column Chromatography*

This technique is one of the most widely used methods for purifying organic compounds on a laboratory scale. When performing chromatography, two immiscible phases are used: a mobile phase and a stationary phase. The products of a reaction are put in contact with these two phases and they undergo a continuous process: there is a dynamic equilibrium of molecules leaving the mobile phase and bind-

ing to the stationary one and molecules doing the opposite. Based on their polarity, different components have different affinities for the two phases. Products that have a higher affinity for the mobile phase move faster than products binding more to the stationary phase: over time, this creates a spatial separation that allows the separation of individual components within the mixture[34]. In the subsequent Sections, column chromatography will be employed: inside a cylindrical piece of glassware, silica is used as the stationary polar phase, while different solvents are employed as mobile phase, depending on the polarities of the products. Highly polar compounds require polar mobile phases, whereas low-polarity compounds require non-polar mobile phases to engender effective separation of the mixture's constituents.

3.1.3 *Nuclear Magnetic Resonance spectroscopy*

Often employed after purification, Nuclear Magnetic Resonance (NMR) spectroscopy is a tool that allows obtaining a signature of the molecule under consideration. Many nuclei possess a spin: when a strong magnetic field is applied to a sample, the nuclei can either align their spin with the field (lower energy state) or against it (higher energy state). The energy gap between these two states increases with the intensity of the field. However, being electrically charged particles, electrons generate another magnetic field while moving. The motion of an electron around a nucleus strongly depends on the electronegativity of the neighboring atoms, and so does the magnetic field they produce. It follows that the gap in energy between the two spin states depends on the chemical environment of the corresponding atom. The energy needed to flip the spin of a nucleus carries information about the nature of the neighboring atoms.
In the NMR spectroscopy employed in this work, hydrogen atoms are analyzed. The NMR spectrometer excites all possible spin transitions frequencies and records the intensity of the de-excitation radiation. The intensity of the de-excitation radiation is plotted as a function of the frequency of the excitation wave. The comparison between the peak values, the frequency of the excitation wave and the profile of the peaks determine the identity of the molecule(s) under study, thanks to an analysis carried out by a software or by the operator [35].

3.2 THE MATERIAL

The fibers simulated in Chapter 2 must satisfy a series of properties: not only do they need to provide electric fields but also they must be stable, biodegradable and not cytotoxic.

Conjugated polymers (polymers having alternating single and double bonds in their backbone) have been proposed to meet those criteria: they can modulate cellular growth [36] and differentiation [37, 38]. However, they suffer from lack of biodegradability and other limiting characteristics [39].
Conjugated oligomers can address some of the issues of conjugated polymers. Following the work of Spicer and colleagues [1], an oligomer with a oligo(3,4-ethylenedioxythiophene) (oligo-EDOT) chain was chosen for the synthesis of the nanofibers. Oligo-EDOT has a defined chemical structure, it is stable, it can be doped (it is redox-active) and it can be made biodegradable.

3.3 DI-CAPPED OLIGO-EDOT DERIVATIVE

Oligo-EDOT-based materials are semiconductors with a relatively low bandgap [40]. Several different ways to synthesize semi-conductive oligomers have been described; in particular, the formation of oligo- and poly-thiophene-based materials has been widely reported. The methods used to form the thiophene chain range from ring-opening polymerization [41] to palladium catalyzed cross-coupling reactions [42]. Oligo-EDOTs can be of larger interest compared to thiophene-based materials, because of their higher conductivity and stability. However, their synthesis is challenging, especially because of the low stability of the material when not oxidized [40]. EDOT is susceptible to singlet electron oxidation to form radicals with maximum orbital coefficients over the carbon atoms adjacent to the sulfur. When a radical forms, the unpaired electron has a high probability to be found over atoms 2 and 5 of the ring, meaning that a radical reaction is most likely to occur at those sites. Previous work from our group has shown that when oligo-EDOTs reach three units, those sites start bonding with each other and an uncontrollable polymerization occurs. In this work, following the methodology laid out by Spicer and colleagues [1], one of the two sites is glyoxylated, as in Figure 17; the oxygen atoms are able to withdraw electrons, making the whole system less reactive, and thus less susceptible to uncontrolled polymerisation.
For what concerns the mechanism of chain formation and extension, the most common option is to employ Stille reaction [43]. However, the stoichiometric use of highly toxic organotin compounds renders this reaction unfeasible for Tissue Engineering applications [44]. Direct arylation is another palladium-catalyzed reaction that presents several advantages, among which a high yield and the lack of an organometallic intermediate, that improves chemocompatibility [45, 46]. The oligo-EDOT chain can be capped with two functional groups; in this work, two short polyethylene glycol (PEG) chains have been added to improve the low solubility of Oligo-EDOT [40].

The final material has a chain of five repeat units, which was found to be the best trade-off between high conductivity (long chain) and high stability (short chain).

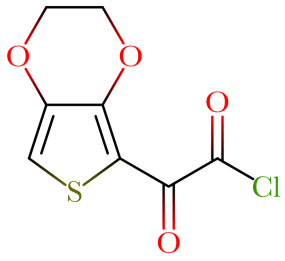

Figure 17: The glyoxylated EDOT: the oxygen atoms pull the electrons away and make the system unreactive

3.4 FOCUS ON THE REACTIONS

Oligo-EDOTs used in this study were synthesised in five steps using an iterative chain extension process, starting with the mono-*N*-protection of 2,2'-(ethylenedioxy)bis(ethylamine) (or simply *Diamine*) by di(tert-butyl) dicarbonate. This renders only one of the two amines available for subseuent reactions, ensuring specific coupling to the EDOT in the subsequent step. Delocalization of the nitrogen lone pair into the adjacent carbonyl group renders it unreactive towards most electrophiles, thereby protecting the latent amine functionality (which can be recovered by deprotection at a later stage) (see Figure 18).

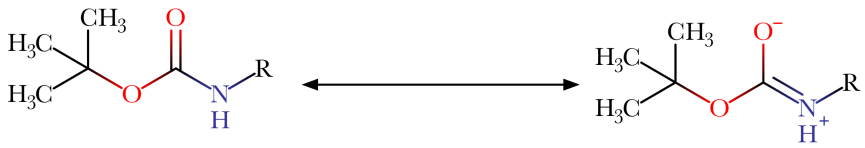

Figure 18: The delocalization that makes the amine group unreactive. The R group can represent any hydrocarbon fragment.

The schematic of the reaction between diamine and Di-tert-butyl dicarbonate (BOC2O) is shown in Figure 19. Because the diamine molecule is symmetric, experimental procedures are optimized to reduce the likelihood of both amines becoming protected (see 3.5 for details).

After the first stage, the glyoxylation of the EDOT is performed in a fashion similar to the method presented by Merkul et al. [47] (Figure 20). The glyoxylated EDOT is then linked to the unprotected site of the diamine, as shown in Figure 21.

To prepare for the EDOT chain formation, it is necessary to introduce a bromine atom, for the oxidative addition of palladium to occur.

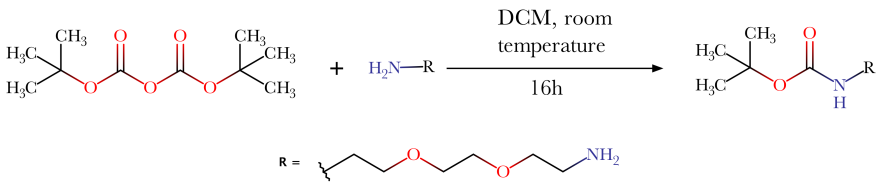

Figure 19: The first reaction of the process, during which one of the amine groups becomes protected by the tert-butyloxycarbonyl group.

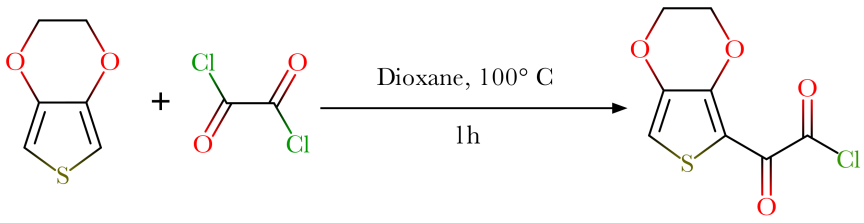

Figure 20: The glyoxylation of the EDOT

Bromination is achieved through a standard procedure, by treating the compound with *N*-bromosuccinimide in DMF [48] (Figure 22).

The direct arylation is performed using the following catalyst and reagents: palladium (II) acetate, pivalic acid, and potassium carbonate. This choice follows the findings of Lafrance and Fagnou [49]: in their work they showed how the yield of direct arylation can drastically improve under these conditions (Figure 23).

The procedure for chain extension is exactly the same: EDOT is brominated and subsequently linked via direct arylation to the rest of the chain. To realize di-capped EDOT, the last element to be added to the chain is a mono-capped brominated EDOT. The effect of glyoxylation endures until the chain has three elements; if a fourth one is added, its radical site is reactive enough to trigger the uncontrolled polymerization. Pentamers can be realized by joining together a dimer and a trimer [1].

3.5 MATERIALS AND METHODS

Mono-BOC-protected Diamine

Commercially available 1,2-Bis(2-aminoethoxy)ethane (here also called *Diamine*) (15 g, 0.1 mol) was added to dichloromethane (DCM) (150 mL). Commercially available Di-tert-butyl dicarbonate (here also called *BOC2O*) (4.58 g, 0.02 mol), was dissolved into DCM (50 mL).
The Diamine solution was added dropwise to the *BOC2O* solution; the mixture was stirred at room temperature for 16 h. The organics was washed with de-ionized water (3 x 150 mL) and with brine (1 x 100 mL), then dried over $MgSO_4$, filtered and concentrated

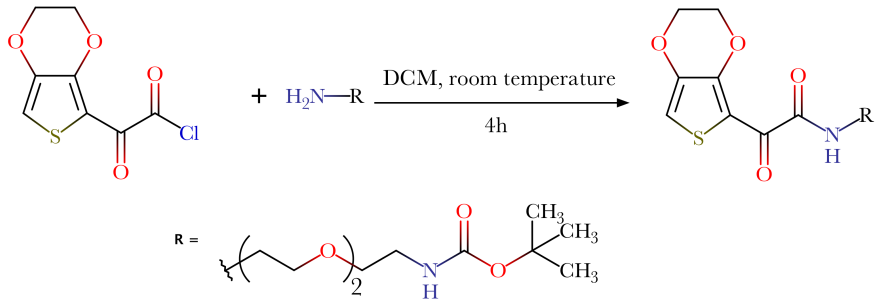

Figure 21: The mono-protected diamine is bonded to the glyoxylated EDOT

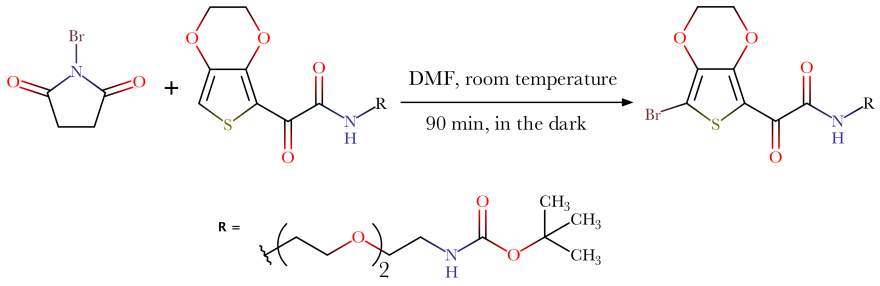

Figure 22: The bromination of the EDOT derivative.

in vacuo. Because mono-protected Diamine is hydrophobic, while the unprotected and di-protected compounds are hydrophilic, the washing procedure was considered sufficient to get rid of the starting materials and the unwanted products. The compound obtained at the end was in the form of a colourless oil (2.89 g, yield of 98.8%). NMR data were consistent with those of literature.

EDOT glyoxylation and capping

Oxalyl Chloride (0.65 mL, 7.58 mmol) was added dropwise to a solution of EDOT (0.81 mL, 7.58 mmol) in dioxane (10 mL). The mixture was heated up to 100 °C for 1 h. After the cooling down at room temperature, this mixture was added dropwise to a solution of the protected diamine (see previous subsection; 2.68 g, 9.16 mmol) and diisopropylethylamine (5.28 mL, 30.32 mmol) in DCM (70 mL). This new mixture was left stirring overnight. The organics were washed with water (1 x 50 mL) and brine (1 x 50 mL), then dried over $MgSO_4$, flitered and concentrated *in vacuo*. The products were purified through flash column cromatography; the starting eluent was initially a 20% (v/v) mixture of Hexane in Ethyl Acetate. The volumetric ratio was then changed to 10% (v/v) and shortly after pure Ethyl Acetate was used. Pure fractions were concetrated *in vacuo*; the prodcuct (2.12 g) was in the form of a yellow oil, with a yield of 57.26%. NMR data were consistent with those of literature.

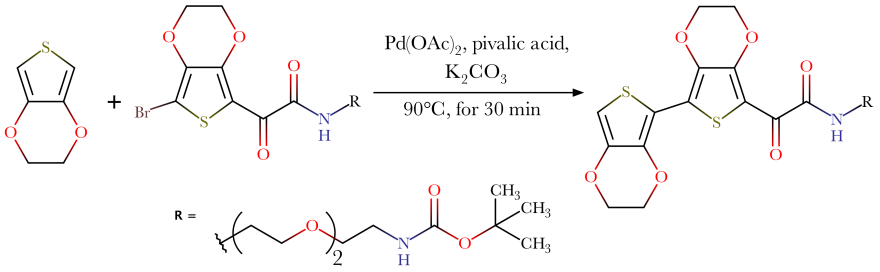

Figure 23: The direct arylation that allows to form the chain of EDOTs

Bromination

The product of the previous step was dissolved in dimethylformamide (DMF) (10 mL). *N*-bromosuccinimide (0.82 g, 4.63 mmol) was then added; the mixture stirred in the dark for 1 h. Afterwards, it was put in de-ionized water (100 mL) and extracted with DCM (200 mL). The organics were washed with hydrochloric acid (2 x 150 mL, 1 M), with brine (1 x 150 mL) and with ethyl acetate (4 x 150 mL) in order to get rid of DMF. They were then dried over $MgSO_4$, filtered and concentrated *in vacuo*. Finally, they were purified by means of flash column chromatography. The eluent was initially a 20% (v/v) mixture of hexane in ethyl acetate; during the process, the volumetric ratio was changed to 10%. The product was in the form of a yellow oil that solidifies on standing (1.449 g a yield of 59%). NMR data were consistent with those of literature.

Chain formation

Brominated oligomer (1 mmol), EDOT (1 mmol), pivalic acid (0.5 m mol), palladium (II) acetate (0.5 mmol) and potassium carbonate (10 mmol) were charged under nitrogen. Dry DMF (2 mL) was added and the mixture heated to 90 °C for 30 min. It was left to cool down at room temperature, then it was diluted with DCM (50 mL) and washed with water (2 x 50 mL) and brine (50 mL). The products were then dried with $MgSO_4$, filtered and concentrated *in vacuo*. The residue was purified by flash column chromatography and pure fractions were again concentrated *in vacuo*. The procedure has been executed by Dr. Christopher Spicer at the Karolinska Institute. NMR data were consistent with those of literature.

Chain extension

The procedure to elongate the chain was a repetition of the ones explained in the two previous subsections. To form a trimer, EDOT was brominated and reacted as in subsection *Chain Formation* with the

EDOT dimer. Dimers and trimers were then joined together in the same fashion. Those procedures have been executed by Dr. Christopher Spicer at the Karolinska Institute.

3.6 CONCLUSIONS

The synthesis of a bench-stable semi-conductive material has been reported. The material was obtained following the protocol of Spicer and colleagues [1]. The glyoxylation of the EDOT prevented an uncontrollable polymerization and the two short PEG chains, capping the EDOT chain, make the material soluble. Moreover, the synthesis did not involve any toxic catalyst; the resulting material is biocompatible and ready to be used for cell stimulation.

4

CELL CULTURE EXPERIMENTS

In this Chapter, the development of a set-up to study the effects of electrical stimulation on pre-osteoblasts is described. This set-up allows measuring the response of cells to electric fields delivered through the oligo-EDOT-based material synthesized in Chapter 3. The response is compared to the one obtained using ITO glass as a conductive substrate; in particular, the proliferation of cells and the mineralization of the extracellular matrix (ECM) are measured. These were meant to validate the work of the previous chapters - in particular, to verify the behavior of cells when stimulated through oligo-EDOT-base nanofibers.

4.1 INTRODUCTION TO THE CELLS AND THE METHODS EMPLOYED

4.1.1 *Stem Cells and Progenitor Cells*

Stem Cells (SCs) are defined as cells with the ability to undergo self-renewal and to give rise to a wide range of differentiated progeny [50]. Progenitors cells (PCs) are usually descendants of SCs; they typically maintain the ability to self-replicate and differentiate, though they can generate a only a very limited number of lineages[51]. The difference between SCs, PCs and differentiated cells resides in the transcription factors (TFs) expressed [52]. TFs are a group of proteins that regulate the transcription of genes inside a cell: they play a crucial role in silencing or enhancing the expression of specific genes, thus giving a unique identity to the cell [53].
Because they can self-renew and produce a range of differentiated descendants, both SCs and PCs are well suited for the field of Tissue Engineering, where they can be employed to regenerate a tissue or restore its function [54, 55]. Therapies involving SCs are now at the stage of clinical trials, with a major focus on treating type I diabetes, heart failure and spinal cord injury [56].
SCs and PCs are also used in other fields; they can be employed as model systems to study diseases or even as an assay for drug discovery [57, 58].

4.1.2 *Osteoblasts and MC3T3-E1 cells*

Osteoblasts are a type of adult cell that synthesizes the bone extracellular matrix (ECM) in a process called osteogenesis [59]. During this

process, they secrete a collagen-proteoglycan matrix that gets calcified by binding to calcium salts, providing hardness and tensile strength to the bone tissue [60].
They are not terminally differentiated cells: if they remain inside the ECM after the calcification, they eventually become osteocytes, cells that regulate the renewal of the bone tissue. If they are pushed towards the outer surface of the bone, they can either undergo apoptosis or become inert bone-lining cells [59]. They work together with osteoclasts, which are responsible for breaking down the bone tissue, in a continuous process of renewal and remodeling [61]
The progenitors of the osteoblasts are the mesenchymal stromal cells (MSCs): those cells can produce a range of differentiated progeny, part of which is represented in Figure 24 [62].

MC3T3-E1 are the cells used in the experiments described in this Chapter. They are a type of adherent and clonal cells with the ability to differentiate into osteoblasts and mineralize the extracellular matrix; because of their differentiation potential and their shape, they can be considered pre-osteoblasts (see scheme 24). They were first isolated by Sudo and colleagues from newborn mouse calvaria [57]. They found that those cells form calcified bone tissue in vitro in a process similar to the osteogenesis occurring in vivo. Because of those characteristics, the authors report that the MC3T3-E1 cell line can be considered a valid model system to study the differentiation of bone cells and calcification of the ECM.
A variety of different subclones exist for MC3T3-E1, with diverse differentiation and mineralization potentials. Following the work of Wang and colleagues [63], subclone 4 was chosen for all the studies, because of the ability to highly mineralize the ECM both in vivo and in vitro.

4.1.3 *Electrical Stimulation in bone Tissue Engineering*

Electrical stimulation affects cell behavior in many different aspects, from differentiation to proliferation to migration: in clinical studies, skin, bone, muscle and nervous tissues can benefit from an electrical stimulus for a faster regeneration [64]. One of the ideal therapeutic approaches involves isolation of cells, expansion and treatment in an in vitro culture, and subsequent transplantation to the treatment site; this approach already leads to very satisfactory results [64, 65]. Thanks to growth factors and specifically designed biomaterials, cell proliferation and differentiation can be precisely controlled in those cultures, making it possible to repair virtually any tissue damage [65].
Another approach that has already been adopted in bone tissue engineering (at the stage of clinical trials) is to directly implant a biomaterial scaffold, able to provide stimuli that promote the healing of the tissue [27]. Growth factors were originally the type of stimulus

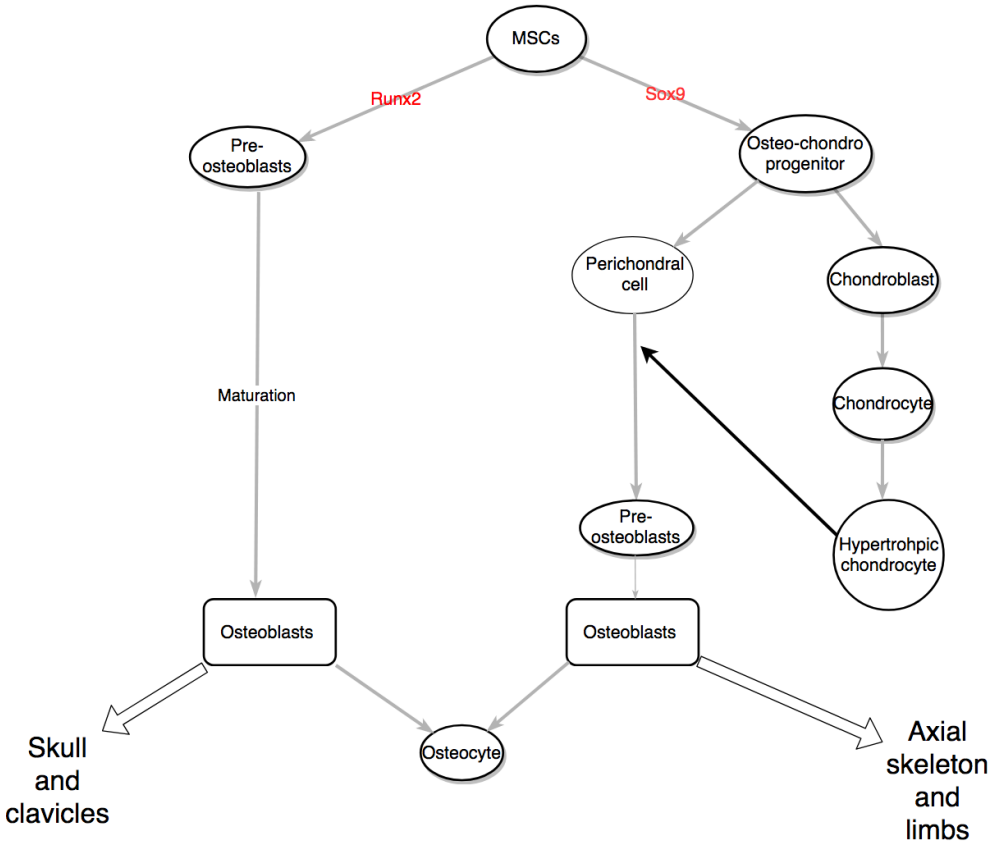

Figure 24: The biogenesis of osteoblasts, according to Rutkovskiy et al. [59]. Depending on which gene is expressed, MSCs can directly become osteoblasts or differentiate into osteo-chondro progenitors (they can also undertake different paths if other transcription factors are expressed: those paths are not shown in the scheme). If pre-osteoblasts stem directly from MSCs, they will give rise to skull and clavicle tissues; if they originate from osteo-chondro progenitors, they will form the axial skeleton and the bones of the extremities. Hypertrophic chondrocytes regulate the differentiation of perichondral cells, but in some cases, they can even become pre-osteoblasts.

intended for these scaffolds, but they have shown a loss of bioactivity once implanted; moreover, they also suffer from poor control over the dose administrated [66]. Other types of stimulus – mechanical or electrical – play an important role in tissue re-growth as well, and scaffolds able to provide them can be of interest [27].
It has been known for a long time that bone tissue shows direct and reverse piezoelectric effect, in a manner similar to a crystalline material [67, 68]: mechanical stimulus results in charge separation. This charge separation can affect a huge variety of different processes and properties, from protein synthesis to membrane permeability, from cell to cell communication to regulation of cell nutrition [67]. The application of an electric field can induce the same effects as the charge separation resulting from a mechanical stimulus: the field can interact with charged molecules and proteins in the membrane or even with charged material inside the cytoplasm [11]. Indeed, electric fields are capable of affecting the expression of osteogenic transcription factors [69], calcium uptake, cell growth [70] and signaling [71] among other processes.

4.2 MATERIALS AND METHODS

For the following studies, mouse fibroblasts ($MC3T3-E1$ subclone 4, ATCC-CRL-2593 obtained from LGC Standards GmbH) have been used. The passage ranged from 6 to 10. The medium used in all the experiments was MEM Alpha (1X, Gibco), with an addition of fetal bovine serum (FBS, 10% v.v., Gibco) and penicillin/streptomycin (1% v.v., Gibco).
The phosphate buffer saline (PBS) used was Dulbecco's PBS (DPBS) with the addition of $CaCl_2$ and $MgCl_2$ (Gibco). The incubator used to store cells was kept at $37\,^{\circ}C$, with 5% of CO_2. The flasks volume was $75\,cm^2$ and cells were cultured until they reached $80-90\%$ confluency. To detach cells, before passaging to another flask or before seeding, trypsin was used (0.05% Ethylenediaminetetraacetic acid (Gibco) – EDTA –, for 2 minutes at $37\,^{\circ}C$). In order to stop the activity of trypsin, medium was added (7 mL), then cells were centrifuged for 5 minutes at 1200 rpm. The cell number was estimated from an aliquot using a hemocytometer. After the centrifugation step, the supernatant was aspirated and the cells were re-suspended in fresh medium to give the appropriate number of cells per volume for the desired seeding density.

4.2.1 *The CyQuant Proliferation Assay*

The CyQuant assay contains a dye that significantly increases its fluorescence upon binding to nucleic acids. Its emission is directly proportional to the cell number, in a wide range of concentrations [72].

For this reason, CyQuant can be used as a proliferation assay. In order for it to work, it is necessary to break the membrane of the cell: this allows the binding of the dye to the nucleic acids. The following protocol (for a 12-well plate) was followed to serve this purpose.
The cell medium is removed from all the wells that will be analyzed. After washing with 1 mL of DPBS, 1 mL of 4% Triton-X-100 (from Sigma-Aldrich) in DPBS is added to each of those wells. Then, the plate is frozen at −70 °C for several days before the final analysis. After a period that ranges between 1 and 4 weeks, samples are thawed. The wells are scraped and their content is mixed using a pipette tip; then the cell lysate is transferred into tubes which are centrifuged for 2 min at 14 rpm. In a 96-well plate 20 µL of the cell lysate are introduced, followed by 180 µL of the following mixture:

- 0.5 µL of CyQuant GR dye
- 10 µL of cell-lysis buffer
- 170 µL of Milli-Q water

200 µL of 0.1% Triton-X 100 are used as negative controls. The fluorescence of the samples is then measured through a microplate reader (in the following experiments, Thermofisher Varioskan LUX). The excitation wavelength is 480 nm and the emission is measured at 520 nm. In the following experiment, all the components of the CyQuant kit by invitrogen are purchased through Thermo-Fisher.

4.2.2 *The Alizarin Red Quantification Assay*

In order to evaluate calcium in the cell culture, Alizarin Red S was used (Sigma-Aldrich, certified by the Biological Stain Commission). This compound is known to react with calcium ions, forming a red precipitate [73]. The following procedure to stain calcium deposits is followed in the subsequent experiments. The cell medium is removed from all the wells. After washing with 1 mL of DPBS, cells are fixed using 1 mL of 3.7% paraformaldehyde in water. After 20 min of fixation cells are washed with 1 mL of de-ionized water, then stained for 10 min with 1 mL of Alizarin Red solution (from Sigma-Aldrich). Each well is then washed three times with 1 mL of de-ionized water. After this stage, pictures are taken for a qualitative assessment of the mineralization (either with a regular camera or with the microscope, as it is done in section 4.4). The mineralization can be evaluated quantitatively by extracting the dye with 1 mL of a 100 mM solution of cetylpyridinium chloride (from Sigma-Aldrich) in water. After 4 h of gentle shaking at room temperature, the absorbance at 540 nm is measured, using blank cetylpyridinium chloride as a negative control. The higher the absorbance, the higher the calcium content.

4.3 OPTIMIZATION OF THE EXPERIMENTAL SET-UP

This Section contains the description of the steps followed to realize a suitable and mechanically stable set-up for the electrical stimulation of cells. Several solutions are proposed, together with their rationale and the relative advantages and drawbacks. Pure ITO glass is used for stimulation, in order reduce the amount of material needed during tests.
The goal of the experiments was to provide electrical stimulation to pre-osteoblasts and quantify its effects: to this end, two analyses are used: the CyQuant and the Alizarin Red quantification assays. The experiments contained the samples stimulated with ITO glass and two different controls (pure ITO glass with no electrical contact and cells without any material). They all appeared in four replicates, in order to have duplicates for each of the two analyses.
The ITO glass worked as an electrode and it remained almost flat to allow for cell adhesion. Counter electrodes are provided in the form of a wire, immersed in the medium. The connection to the voltage generator happens inside the incubator and it is realized through wires and crocodile connectors. It is schematically represented in Figure 25. The wires reach the plate through a small opening on the back of the incubator, while the cable connection to the voltage generator remains outside.

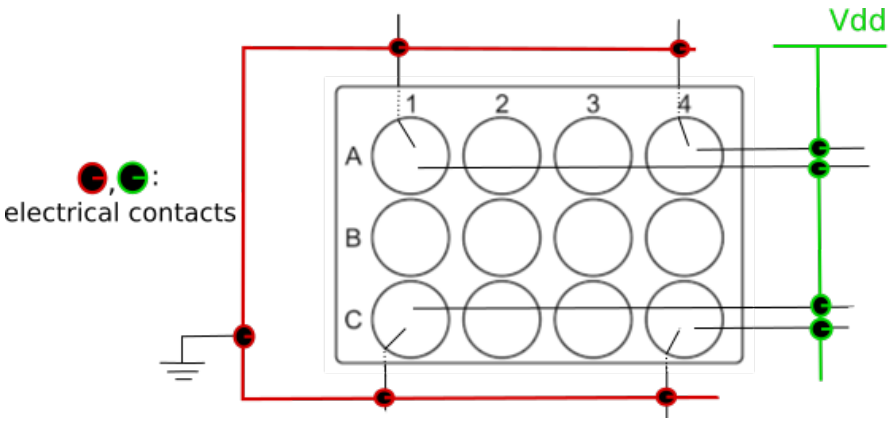

Figure 25: Schematic of the connections. The coloured lines represent wires, the circles are representing the crocodile connectors and the thin black lines are the needles, the final element in the chain from the voltage generator to the ITO glass.

4.3.1 *Platinum wires underneath the lid*

The first and most simple idea is to have platinum wires pass under the lid. Their thin diameter (0.25 mm) allows the lid to close almost perfectly (Figure 26).

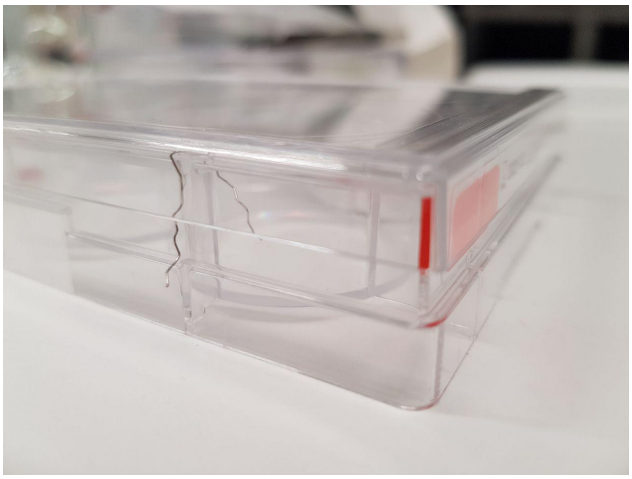

Figure 26: A platinum wire passing underneath the lid of a 12-well plate

They stick to the ITO glass thanks to parafilm, and they protrude outwards so that they can be connected to the voltage generator. The wires used as counter electrodes follow a similar path, but their short length allows them to remain at a distance from the electrodes.
Beside the problems related to parafilm, discussed in subsection 4.3.2, this solution consumes a significative amount of platinum: for this reason, efforts have been made to realize a more compact structure, able to minimize the length of the wires.

4.3.2 *Platinum wires through the lid*

The amount of platinum needed can be drastically reduced by having wires follow a straight path (no turns, coils or other lengthy features). One way to implement this idea is to drill holes through the lid: the wires can reach the ITO glass and still protrude upwards, in order to be connected to the rest of the circuit. This idea is represented in Figure 27.

In addition, platinum wires for counter electrodes are substituted with needles made of steel (Sterican by Braun, 0.8 mm in diameter): at this stage, they still follow the path described in the previous subsection. Holes are drilled by heating up a needle (again, Sterican by Braun, 0.8 mm in diameter) for 3 s in the flame of a gas torch. The hot needle is pressed against the lid, where it penetrates the structure with ease. While this system represents an improvement compared to the previous one, it still suffers from the use of parafilm. Employing ethanol (either liquid or spray), as a mandatory sterilization procedure before inserting anything in the cell hood, undermines the adhesiveness of the film; the process of connecting the wires to the generator is harsh enough to detach the glass from the wires.
Superglue (by Loctite) has been used in the attempt to solve this problem; however, even if the stiction of the platinum wire to the glass

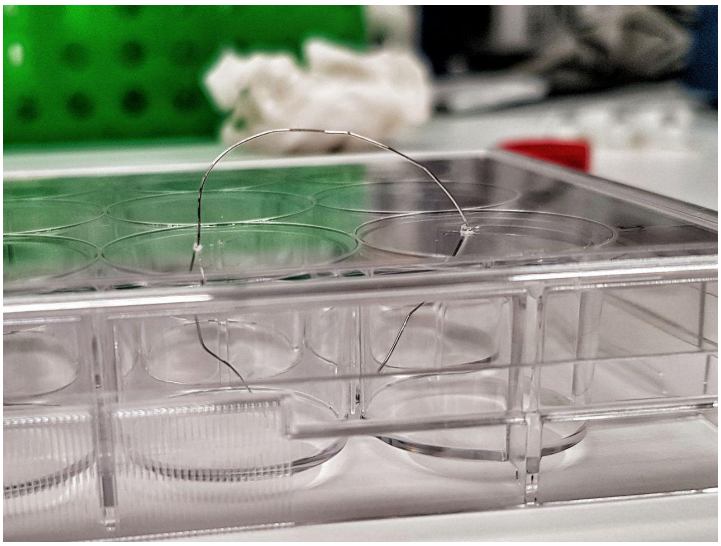

Figure 27: Platinum wire passing through the lid. It would be possible to minimize the wire consumption even more by avoiding the arch, but the number of crocodile connectors is limited, and it is not possible to connect all the samples individually.

seems to be adequate, as soon as the two are immersed in the cell medium they detach.

4.3.3 *Needles through the lateral walls*

Practical tests of the above mentioned structures have shown that the most critical point (where the structure usually fails) is the connection to the voltage generator. The crocodile connectors are heavy compared to the rest of the system and the space to work in is limited. It is therefore necessary to create a mechanically stable structure, able to withstand the connection procedure. The thin platinum wires are not a good candidate for such a system: even though their electrical properties are far superior to the ones of steel needles, they break and deform too easily.
There are two lateral walls that separate the inside of a well from the outside world. If a needle passes through both of them, the two narrow holes together are able to firmly keep the structure in place: as a test, it is possible to push or pull the whole plate holding on to the needle, without having it slide relative to the plate. Nevertheless, it is still possible to rotate it inside the holes. The system consisting of a stable wire inside the plate is represented in Figure 28.
Then, a fragment of ITO glass is put inside the well, so that it rests horizontally, as in Figure 29. Now, if the length of the segment s is chosen properly, the needle cannot complete a full turn: the holes and the upper surface of the glass are too close to each other. If it is forced to slide until it comes to a stop, the needle remains locked in place

thanks to the pressure exerted by the glass and the holes: this creates a stable system.

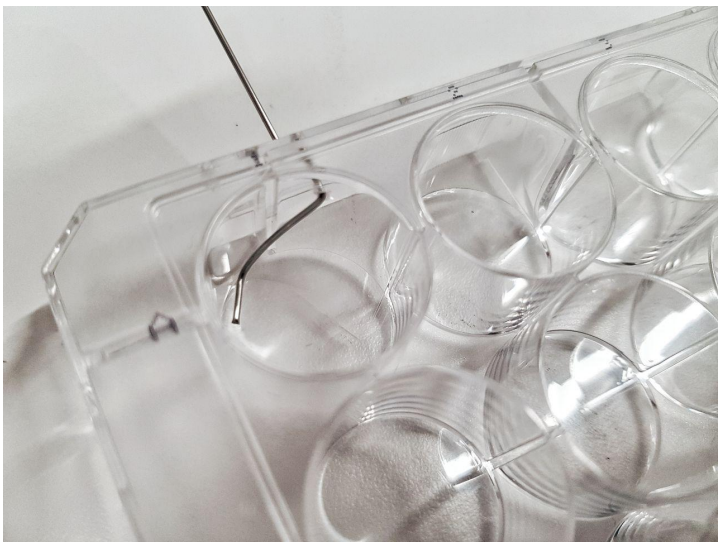

Figure 28: A needle passing through two walls of the plate. The structure is stable and the needle is securely in place.

For further stability, the counter electrodes rest on top of the lid, pass through it and then reach the medium, as represented in Figure 30.

4.3.4 *Test of the final experimental set-up*

As shown in Figure 25, rectangular fragments of ITO glass were placed in rows A and C of a 12-well plate. MC3T3-E1 cells were seeded in every well at a density of 15000 cells/cm^2. Electrical stimulation was provided to the four wells in the corners (A1, A4, C1, C4), using the glass being grounded and the counter electrode at 1 V, with the set-up described in subsection 4.3.3.
After 7 d the plate was disconnected from the voltage source and the mineralization assays was performed as described in subsections 4.2.1 and 4.2.2. The electrical stimulation seems not to have affected the mineralization process. The test confirmed that cells can mineralize the ECM on top of ITO glass, but it is hard to see any difference between the stimulated and the unstimulated samples (Figure 31).

4.4 CELL CULTURE ON OLIGO-EDOTS

4.4.1 *Materials and methods*

Four thin samples made of Oligo-EDOT (trimers) were placed on top of four ITO glass fragments. Those fragments were put in the four corners of a 12-well plate (wells A1, A4, C1, C4); ITO glass fragments

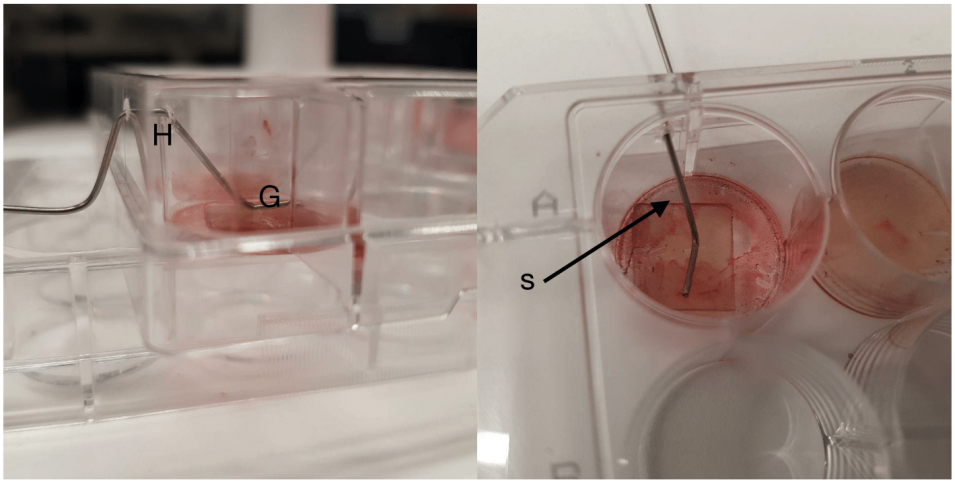

Figure 29: The needle in Figure b) cannot move further to the left because segment s is longer than the distance between point H and the contact point G in Figure a). At this point the needle cannot slide anymore and the system is stable.

without any material were inserted in wells A2, A3, C2, C3 while row B was left empty (Figure 25 for reference).
MC3T3-E1 cells were seeded in every well at a density of 15000 cells/cm^2. Electrical stimulation was provided to all the wells in row A and C, with the glass being grounded and the counter electrode at 1 V, using the technique described in subsection 4.3.3.
After 10 d the plate was disconnected from the voltage source.
Alizarin Red and CyQuant assays were carried out as explained in subsection 4.2.2 and 4.2.1.

4.4.2 *Results*

Two of the four wells containing the oligo-EDOT samples showed a brown color (Figure 32, A1 and A4).

The reason for this unexpected finding is probably to be attributed to the degradation of the material. In fact, well A1 (top left corner) was heavily scratched by the needle during the connection to the generator, and this has probably impared the functionality the sample. In well A4 (top right corner) the ITO glass was tilted and it possibly came in contact with the counter electrode, forming a short circuit. The results obtained from the assays carried out in the brown-colored wells (almost no mineralization and proliferation) were discarded.
The mineralization on the other stimulated sample is much more pronounced than the one found on ITO glass and in the unstimulated wells (Figures 33 and 34).

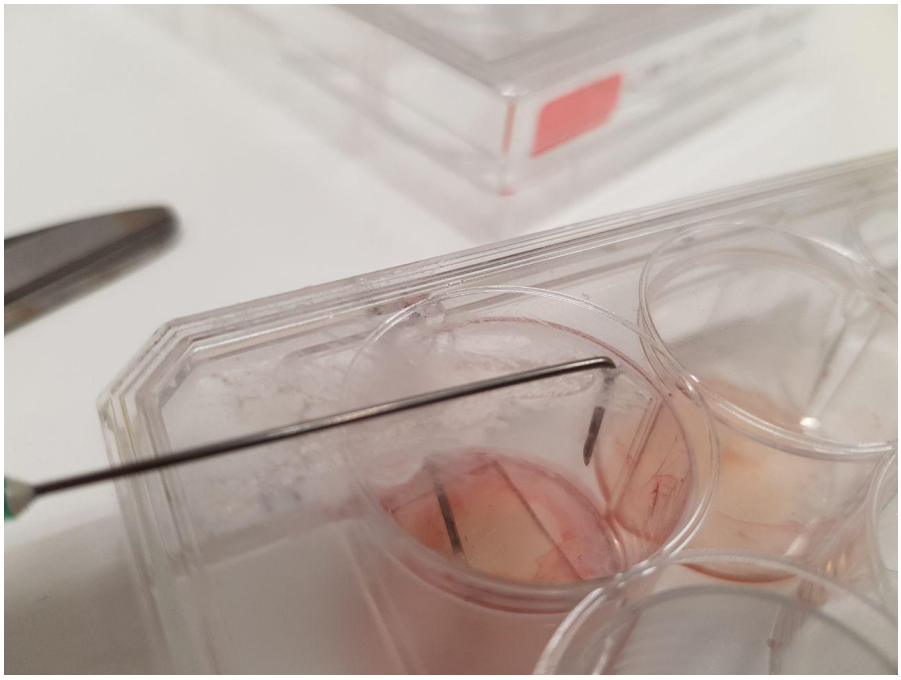

Figure 30: The counter electrode, represented by the steel needle, reaches the inside of the well passing through a hole in the lid

Quantitative analysis shows that the mineralization is ≈ 2.6 times higher when cells are stimulated using the oligo-EDOTs (Figure 35).

In comparison to the wells stimulated through ITO glass, the proliferation in the well containing the material (not degraded) was ≈ 1.4 times higher (Figure 36).

4.4.3 *Discussion*

When osteoblasts are provided with a stimulus delivered through conductive polymers, their proliferation and the mineralization of the ECM increase [7, 8].
The results obtained are promising and follow those expectations. However, the increase in mineralization might be simply due to the presence of more nucleation sites on the material compared to the pure glass. If this hypothesis was confirmed, the electrical stimulation would not be responsible for the increased mineralization and it would not be possible to conclude anything on the electrical properties of the material. A further test is necessary, in order to compare the mineralization on stimulated and unstimulated oligo-EDOT-based materials. Moreover, it is necessary to repeat the tests several times in order to draw quantitative conclusions on the behavior of cells. Unfortunately, because of the limited amount of time and samples, this is left as a future work.

For what concerns the CyQuant proliferation assay, the values are far from being clear. Only one well containing the material was us-

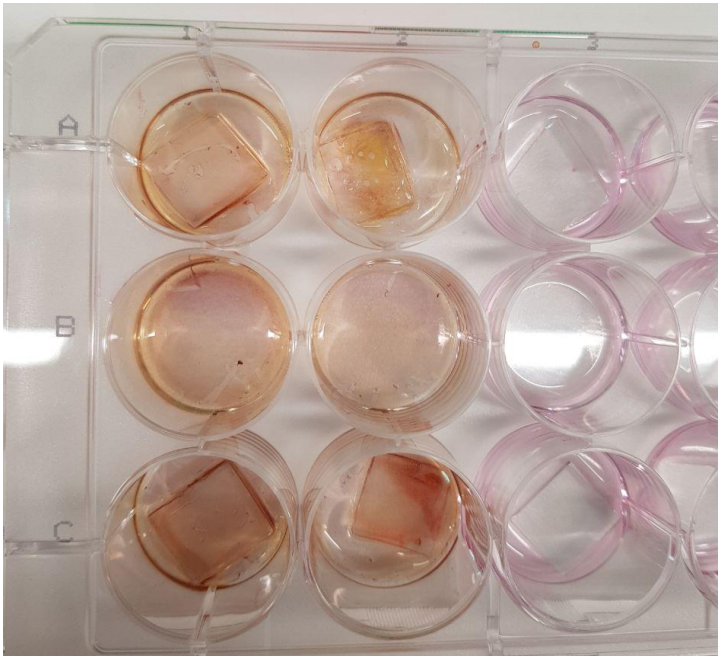

Figure 31: The results of the mineralization assay (first two columns on the left) of the experiment described in subsection 4.3.4. Samples stimulated by ITO glass are in the corners, cells with no glass in the central row and cells on unstimulated ITO glass are in the remaining wells (A2 and C2)

able; moreover, the huge values of the standard deviation make the results debatable. Previous tests have shown how the outcome of the CyQuant assay strongly depends on the technical procedure undertaken. The presence of the material and the ITO glass – of different dimensions and shapes – renders the process difficult to replicate, thus the results show significant fluctuations. For the same reason, the unstimulated control was not included in the assay: the lack of a piece of glass in the well makes the procedure completely different. It was not considered comparable with the other two.

4.5 CONCLUSIONS

In this section, the effects of electrical stimulation provided through oligo-EDOT-based nanofibers were analyzed. The first obstacle was the development of a suitable set-up; a stable and robust system has been achieved by drilling several holes inside a 12-well plate and employing steel needles as wires. Electrical stimulation was provided through ITO glass and Oligo-EDOT-based materials, whose synthesis has been presented in Chapter 3. The results indicate that the mineralization is drastically increased thanks to the presence of the synthesized material ($\approx$ 2.6 times), but further analyses must be carried out to determine the role played by the electrical stimulation in

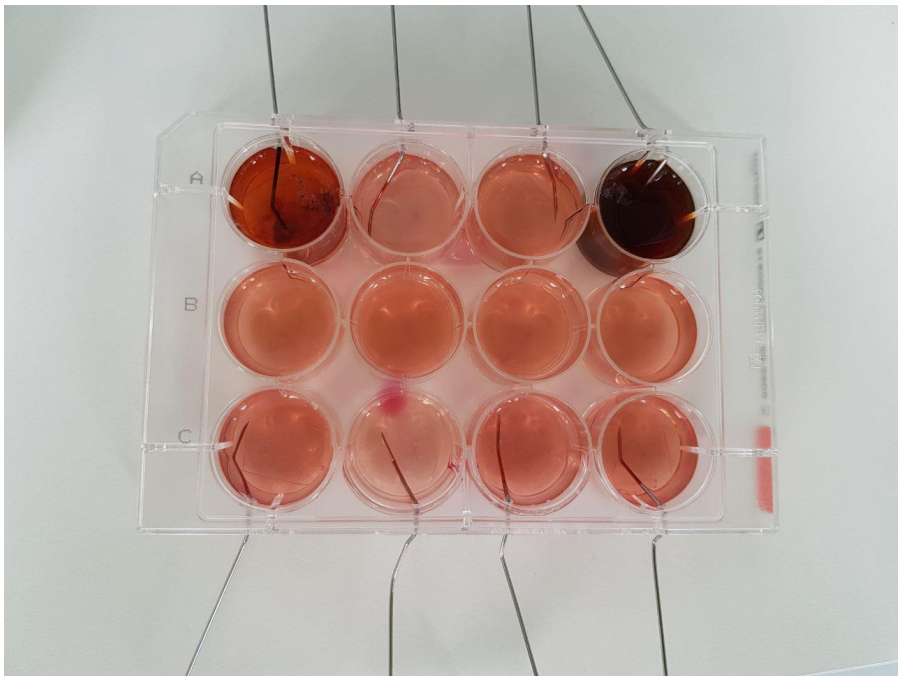

Figure 32: The well plate for the experiment of Section 4.4, after 10 d of electrical stimulation

this increase. Also, the proliferation seems to increase thanks to the presence of the material ($\approx$ 1.4 times). However, the results are still debatable due to the high variability of the experiment, and further tests are needed to confirm or contradict these findings.

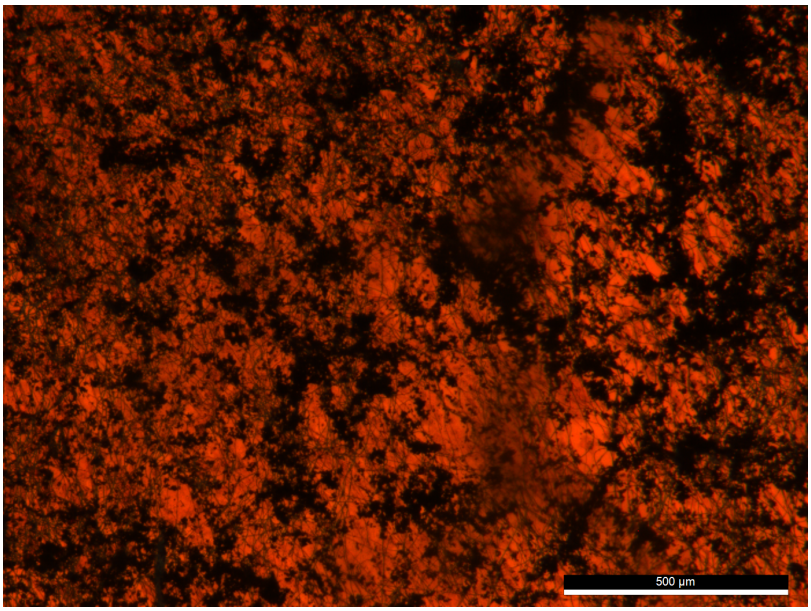

Figure 33: The results of Alizarin Red assay on the EDOT-based material. The mineral crystals (in dark colour) are large and expanded.

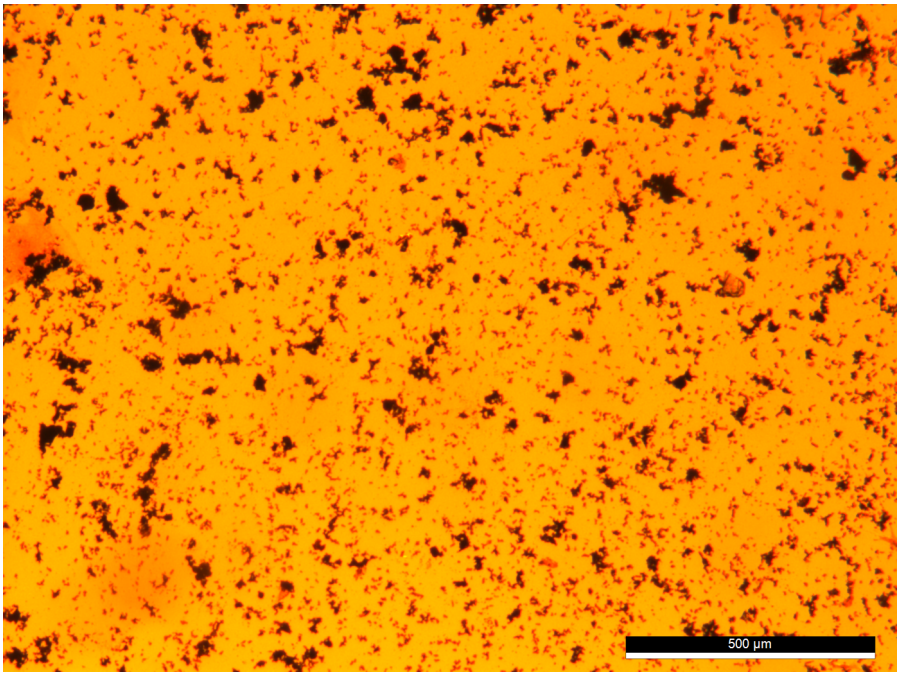

Figure 34: The result of Alizarin Red assay on ITO glass. The crystals of minerals are tiny and the mineralization appears more scarce than in Figure 33.

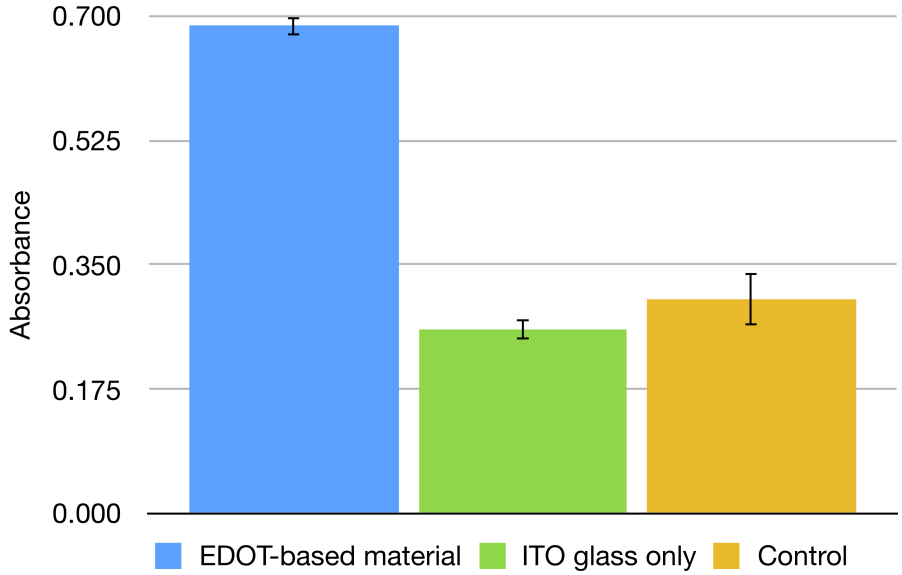

Figure 35: Absorbance of solubilized Alizarin Red mineral stains from MC3T3-E1 cells cultured for 10 d on EDOT-based material on ITO glass (blue), on ITO glass only (green) and on cell culture plastic as a control (orange). The error bars represent the standard deviation.

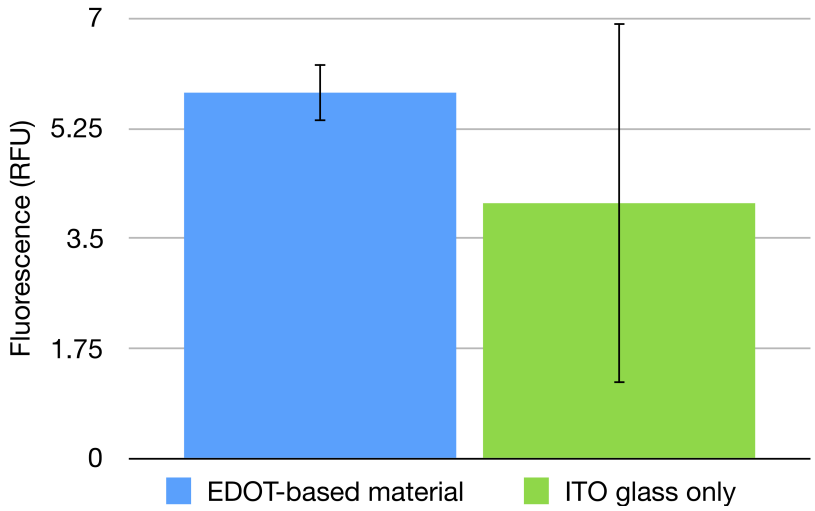

Figure 36: Fluorescence of the cell lysate bound to the CyQuant GR dye. The lysate was obtained from MC3T3-E1 cells stimulated for 10 d using EDOT-based material on ITO glass (blue) and ITO glass only (green). The error bars represent the standard deviation.

BIBLIOGRAPHY

[1] C. D. Spicer et al. "Synthesis of Hetero-bifunctional, End-Capped Oligo-EDOT Derivatives." In: *Chem* 2.1 (2017), pp. 125–138. ISSN: 24519294.

[2] O. V. Salata. "Applications of nanoparticles in biology and medicine." In: *Journal of Nanobiotechnology* 2 (2004), p. 3. ISSN: 1477-3155.

[3] J. Shi et al. "Nanotechnology in Drug Delivery and Tissue Engineering: From Discovery to Applications." In: *Nano letters* 10.9 (2010), pp. 3223–3230. ISSN: 1530-6984.

[4] M. Goldberg, R. Langer, and X. Jia. "Nanostructured materials for applications in drug delivery and tissue engineering." In: *Journal of biomaterials science. Polymer edition* 18.3 (2007), pp. 241–268. ISSN: 0920-5063.

[5] R. Balint, N. J. Cassidy, and S. H. Cartmell. "Electrical stimulation: a novel tool for tissue engineering." eng. In: *Tissue engineering. Part B, Reviews* 19.1 (2013), pp. 48–57. ISSN: 1937-3376 (Electronic).

[6] L. Leppik et al. "Combining electrical stimulation and tissue engineering to treat large bone defects in a rat model." In: *Scientific Reports* 8.1 (2018), p. 6307. ISSN: 2045-2322.

[7] M. R. Love et al. "Effects of electrical stimulation on cell proliferation and apoptosis." In: *Journal of Cellular Physiology* 233.3 (2018), pp. 1860–1876. ISSN: 10974652.

[8] S. Meng, Z. Zhang, and M. Rouabhia. "Accelerated osteoblast mineralization on a conductive substrate by multiple electrical stimulation." In: *Journal of Bone and Mineral Metabolism* 29.5 (2011), pp. 535–544. ISSN: 1435-5604.

[9] D. Logan. *A First Course in the Finite Element Method*. Ed. by Cl-Engineering. 5th ed. 2010. ISBN: 978-0495668251.

[10] W. B. J. Zimmerman. "Introduction to COMSOL Multiphysics." In: *Multiphysics Modeling with Finite Element Methods*. World Scientific Publishing Company, 2006. Chap. 1, pp. 1–26.

[11] T. Taghian, D. A. Narmoneva, and A. B. Kogan. "Modulation of cell function by electric field : a high-resolution analysis." In: *J. R. Soc. Interface* 12.20150153 (2015).

[12] H. Fricke. "The Electric Permittivity of a Dilute Suspension of Membrane-Covered Ellipsoids." In: *Journal of Applied Physics* 24.5 (1953), pp. 644–646. ISSN: 0021-8979.

[13] J. Gimsa and D. Wachner. "Analytical description of the transmembrane voltage induced on arbitrarily oriented ellipsoidal and cylindrical cells." In: *Biophysical Journal* 81.4 (2001), pp. 1888–1896. ISSN: 00063495.

[14] "The electrostatic interface." In: *COMSOL Multiphysics Reference Manual, version 4.3*. COMSOL Inc, pp. 583–591.

[15] A. C Fisher. "The Electrical Double Layer." In: *Electrochemistry Teaching Notes*. University of Cambridge, 2010.

[16] M. Paunovic and M. Schlesinger. *Fundamentals of electrochemical deposition*. 1st ed. Wiley, 1998. ISBN: 0-471-16820-3.

[17] M. Z. Bazant, K. T. Chu, and B. J. Bayly. "Current-Voltage Relations for Electrochemical Thin Films." In: *Siam Journal of Applied Mathematics* 65.5 (2004), pp. 1463–1484. ISSN: 0036-1399.

[18] D. J. Griffiths. *Introduction to Electrodynamics*. 3rd ed. PHI Learning, 2009, p. 576. ISBN: 8120316010.

[19] B. Alberts, A Johnson, and J Lewis. "Integrins." In: *Molecular Biology of the Cell*. 4th ed. New York: Garland Science, 2002.

[20] M. R. Cho et al. "Induced redistribution of cell surface receptors by alternating current electric fields." In: *The FASEB Journal* 8.10 (1994), pp. 771–776. ISSN: 0892-6638.

[21] M. R. Hanlon and B. A. Wallace. "Structure and Function of Voltage-Dependent Ion Channel Regulatory β Subunits." In: *Biochemistry* 41.9 (2002), pp. 2886–2894. ISSN: 0006-2960.

[22] D. Purves, G. Augustine, and D. Fitzpatrick. "Voltage-Gated Ion Channels." In: *Neuroscience*. 2nd ed. Sunderland (MA): Sinauer Associates, 2001.

[23] A. Mugler et al. "Membrane Clustering and the Role of Rebinding in Biochemical Signaling." In: *Biophysical Journal* 102.5 (2012), pp. 1069–1078. ISSN: 0006-3495.

[24] K. Takahashi, S. Tănase-Nicola, and P. R. ten Wolde. "Spatio-temporal correlations can drastically change the response of a MAPK pathway." In: *Proceedings of the National Academy of Sciences of the United States of America* 107.6 (2010), pp. 2473–2478. ISSN: 0027-8424.

[25] H. L. Zhang and H. B. Peng. "Mechanism of Acetylcholine Receptor Cluster Formation Induced by DC Electric Field." In: *PLoS ONE* 6.10 (2011). Ed. by H. Pant, e26805. ISSN: 1932-6203.

[26] K. J. Mcleod and C. T. Rubin. "The Effect of Low-Frequency on Osteogenesis." In: *The Journal of Bone and Joint Surgery* 8 (1992), pp. 920–929.

[27] J. Ramirez-Vick. "Biophysical Stimulation for Bone Regeneration." In: *JSM Biotechnol Biomed Eng* 1.2 (2013), pp. 247–253. ISSN: 08966273.

[28] T. R. Brumleve and R. P. Buck. "Numerical solution of the Nernst-Planck and poisson equation system with applications to membrane electrochemistry and solid state physics." In: *Journal of Electroanalytical Chemistry* 90.1 (1978), pp. 1–31. ISSN: 00220728.

[29] A. Kisza. "The capacitance of the electric double layer of electrodes in molten salts." In: *Journal of Electroanalytical Chemistry* 534.2 (2002), pp. 99–106. ISSN: 00220728.

[30] K. R. Foster. "Thermal and nonthermal mechanisms of interaction of radio-frequency energy with biological systems." In: *IEEE Transactions on Plasma Science* 28.1 (2000), pp. 15–23. ISSN: 00933813.

[31] J. Miyakoshi. "Cellular and molecular responses to radio-frequency electromagnetic fields." In: *Proceedings of the IEEE* 101.6 (2013), pp. 1494–1502. ISSN: 00189219.

[32] J. Hartwig. *Organotransition Metal Chemistry: From Bonding to Catalysis*. 1st ed. University Science books, 2009. ISBN: 189138953X.

[33] J. Wolfe and J. J. Li. "An introduction to palladium catalysis." In: *Palladium in Heterocyclic Chemistry*. Ed. by J. J. Li and G. W.B.T.T.O.C. S. Gribble. Vol. 26. Elsevier, 2007, pp. 1–35. ISBN: 1460-1567.

[34] J. Gilbert and S. Martin. "Chromatography." In: *Experimental Organic Chemistry*. 5th ed. Cengage Learning, 2011. Chap. 6.

[35] J. Clayden, N. Greeves, and S. Warren. "Determining Organic structures." In: *Organic Chemistry*. 2nd ed. Oxford University Press, 2012. Chap. 3. ISBN: 9780199270293.

[36] J. Y. Wong, R. Langer, and D. E. Ingber. "Electrically conducting polymers can noninvasively control the shape and growth of mammalian cells." In: *Proceedings of the National Academy of Sciences* 91.8 (1994), pp. 3201–3204. ISSN: 0027-8424.

[37] K. J. Gilmore et al. "Skeletal muscle cell proliferation and differentiation on polypyrrole substrates doped with extracellular matrix components." In: *Biomaterials* 30.29 (2009), pp. 5292–5304. ISSN: 0142-9612.

[38] N. Srivastava et al. "Neuronal Differentiation of Embryonic Stem Cell Derived Neuronal Progenitors Can Be Regulated by Stretchable Conducting Polymers." In: *Tissue Engineering. Part A* 19.17-18 (2013), pp. 1984–1993. ISSN: 1937-3341.

[39] N. K. Guimard, N. Gomez, and C. E. Schmidt. "Conducting polymers in biomedical engineering." In: *Progress in Polymer Science (Oxford)* 32.8-9 (2007), pp. 876–921. ISSN: 00796700.

[40] J. J. Apperloo et al. "Optical and redox properties of a series of 3,4-ethylenedioxythiophene oligomers." In: *Chemistry - A European Journal* 8.10 (2002), pp. 2384–2396. ISSN: 09476539.

[41] K. Takamizu and K. Nomura. "Synthesis of Oligo(thiophene)-Coated Star-Shaped ROMP Polymers: Unique Emission Properties by the Precise Integration of Functionality." In: *Journal of the American Chemical Society* 134.18 (2012), pp. 7892–7895. ISSN: 0002-7863.

[42] L. Zhang, N. Colella, and F. Liu. "Synthesis, Electronic Structure, Molecular Packing/Morphology Evolution, and Carrier Mobilities of Pure Oligo-/Poly (alkylthiophenes)." In: *Journal of the American Chemical Society* (2012).

[43] B. Carsten et al. "Stille polycondensation for synthesis of functional materials." In: *Chemical Reviews* 111.3 (2011), pp. 1493–1528. ISSN: 00092665.

[44] K. A. Winship. "Toxicity of tin and its compounds." eng. In: *Adverse drug reactions and acute poisoning reviews* 7.1 (1988), pp. 19–38. ISSN: 0260-647X (Print).

[45] C. Gozzi et al. "Direct thiophene arylation catalysed by palladium." In: *Tetrahedron Letters* 38.51 (1997), pp. 8867–8870. ISSN: 00404039.

[46] D. J. Schipper and K. Fagnou. "Direct Arylation as a Synthetic Tool for the Synthesis of Thiophene-Based Organic Electronic Materials." In: *Chemistry of Materials* 23.6 (2011), pp. 1594–1600. ISSN: 0897-4756.

[47] E. Merkul et al. "Three-Component Synthesis of Ynediones by a Glyoxylation/Stephens-Castro Coupling Sequence." In: *Angewandte Chemie International Edition* 50.13 (2011), pp. 2966–2969. ISSN: 14337851.

[48] R. H. Mitchell, Y.-H. Lai, and R. V. Williams. "N-Bromosuccinimide-dimethylformamide: a mild, selective nuclear monobromination reagent for reactive aromatic compounds." In: *The Journal of Organic Chemistry* 44.25 (1979), pp. 4733–4735. ISSN: 0022-3263.

[49] M. Lafrance and K. Fagnou. "Palladium-catalyzed benzene arylation: Incorporation of catalytic pivalic acid as a proton shuttle and a key element in catalyst design." In: *Journal of the American Chemical Society* 128.51 (2006), pp. 16496–16497. ISSN: 00027863.

[50] A. C. Brignier and A. M. Gewirtz. "Embryonic and adult stem cell therapy." In: *Journal of Allergy and Clinical Immunology* 125.2, Supplement 2 (2010), S336–S344. ISSN: 0091-6749.

[51] R. Lanza and A. B. T. Atala. "Chapter 2 - 'Stemness': Definitions, Criteria, and Standards." In: *Essentials of Stem Cell Biology*. 3rd ed. Boston: Academic Press, 2014, pp. 7–17. ISBN: 978-0-12-409503-8.

[52] G. Pan et al. "A negative feedback loop of transcription factors that controls stem cell pluripotency and self-renewal." In: *The FASEB Journal* 20.10 (2006), pp. 1730–1732. ISSN: 0892-6638.

[53] T. Phillips and L. Hoopes. "Transcription factors and transcriptional control in eukaryotic cells." In: *Nature Education* (2008).

[54] K. G. Sylvester and M. T. Longaker. "Stem cells: Review and update." In: *Archives of Surgery* 139.1 (2004), pp. 93–99. ISSN: 0004-0010.

[55] R Langer and J. P. Vacanti. "Tissue engineering." In: *Science* 260.5110 (1993), pp. 920 –926.

[56] E. A. Kimbrel and R. Lanza. "Current status of pluripotent stem cells: moving the first therapies to the clinic." In: *Nature Reviews Drug Discovery* 14 (2015), p. 681.

[57] H. Sudo et al. "In vitro differentiation and calcification in a new clonal osteogenic cell line derived from newborn mouse calvaria." In: *Journal of Cell Biology* 96.1 (1983), pp. 191–198. ISSN: 00219525.

[58] J. D. McNeish. "Stem cells as screening tools in drug discovery." In: *Current Opinion in Pharmacology* 7.5 (2007), pp. 515–520. ISSN: 1471-4892.

[59] A. Rutkovskiy, K.-O. Stensløkken, and I. J. Vaage. "Osteoblast Differentiation at a Glance." In: *Medical Science Monitor Basic Research* 22 (2016), pp. 95–106. ISSN: 2325-4416.

[60] S. Gilbert. "Osteogenesis: The Development of Bones." In: *Developmental Biology*. 6th ed. Sunderland (MA), 2000.

[61] N. A. Sims and T. J. Martin. "Coupling Signals between the Osteoclast and Osteoblast: How are Messages Transmitted between These Temporary Visitors to the Bone Surface?" In: *Frontiers in Endocrinology* 6 (2015), p. 41. ISSN: 1664-2392.

[62] E. Densen, R. Gopalakrishnan, and J. Westendorf. "Regulation of gene expression in osteoblasts." In: *BioFactors* 36.1 (2010), pp. 25–32. ISSN: 0951-6433.

[63] D. Wang et al. "Isolation and Characterization of MC3T3-E1 Vivo Differentiation / Mineralization Potential *." In: *Journal of Bone and Mineral Research* 14.6 (1999), pp. 893–903.

[64] S. Mobini, L. Leppik, and J. H. Barker. "Direct current electrical stimulation chamber for treating cells in vitro." In: *BioTechniques* 60.2 (2016), pp. 95–98. ISSN: 19409818.

[65] R. Cancedda et al. "Tissue engineering and cell therapy of cartilage and bone." In: *Matrix Biology* 22 (2003), pp. 81–91. ISSN: 0945053X.

[66] K. Lee, E. A. Silva, and D. J. Mooney. "Growth factor delivery-based tissue engineering: general approaches and a review of recent developments." In: *Journal of The Royal Society Interface* 8.55 (2011), 153 LP –170.

[67] C. Basset, R. Pawluk, and A. Pilla. "Acceleration of fracture repair by electromagnetic fields. A surgically noninvasive method." In: *Ann N Y Acad Sci.* 238 (1974), pp. 242–262.

[68] E. Fukada and I. Yasuda. "On the Piezoelectric Effect of Bone." In: *Journal of the Physical Society of Japan* 12.10 (1957), pp. 1158–1162. ISSN: 0031-9015.

[69] Y. Yong et al. "EMF acts on rat bone marrow mesenchymal stem cells to promote differentiation to osteoblasts and to inhibit differentiation to adipocytes." In: *Bioelectromagnetics* 31.4 (2009), pp. 277–285. ISSN: 0197-8462.

[70] H. Ozawa et al. "Electric Fields Stimulate DNA Synthesis of Mouse Osteoblast-Like Cells (MC3T3-El) by a Mechanism Involving Calcium Ions." In: *Journal of Cellular Physiology* 138 (1989), pp. 477–483.

[71] T. Bodamyali et al. "Pulsed Electromagnetic Fields Simultaneously Induce Osteogenesis and Upregulate Transcription of Bone Morphogenetic Proteins 2 and 4 in Rat Osteoblastsin Vitro." In: *Biochemical and Biophysical Research Communications* 250.2 (1998), pp. 458–461. ISSN: 0006-291X.

[72] L. J. Jones et al. "Sensitive determination of cell number using the CyQUANT® cell proliferation assay." In: *Journal of Immunological Methods* 254.1-2 (2001), pp. 85–98. ISSN: 00221759.

[73] H. Pucthler, S. N. Meloan, and M. S. Terry. "On the history and mechanism of alizarin and alizarin red S stains for calcium." In: *Journal of Histochemistry & Cytochemistry* 17.2 (1969), pp. 110–124. ISSN: 0022-1554.

COLOPHON

This document was typeset using the typographical look-and-feel `classicthesis` developed by André Miede. The style was inspired by Robert Bringhurst's seminal book on typography *"The Elements of Typographic Style"*. `classicthesis` is available for both LaTeX and LyX:

https://bitbucket.org/amiede/classicthesis/